TRISO Fuel: Properties and Failure Modes

June 2021

BE Wells
NR Phillips
KJ Geelhood

DISCLAIMER

This report was prepared as an account of work sponsored by an agency of the United States Government. Neither the United States Government nor any agency thereof, nor Battelle Memorial Institute, nor any of their employees, makes **any warranty, express or implied, or assumes any legal liability or responsibility for the accuracy, completeness, or usefulness of any information, apparatus, product, or process disclosed, or represents that its use would not infringe privately owned rights**. Reference herein to any specific commercial product, process, or service by trade name, trademark, manufacturer, or otherwise does not necessarily constitute or imply its endorsement, recommendation, or favoring by the United States Government or any agency thereof, or Battelle Memorial Institute. The views and opinions of authors expressed herein do not necessarily state or reflect those of the United States Government or any agency thereof.

PACIFIC NORTHWEST NATIONAL LABORATORY
operated by
BATTELLE
for the
UNITED STATES DEPARTMENT OF ENERGY
under Contract DE-AC05-76RL01830

Printed in the United States of America

Available to DOE and DOE contractors from the
Office of Scientific and Technical Information,
P.O. Box 62, Oak Ridge, TN 37831-0062;
ph: (865) 576-8401
fax: (865) 576-5728
email: reports@adonis.osti.gov

Available to the public from the National Technical Information Service
5301 Shawnee Rd., Alexandria, VA 22312
ph: (800) 553-NTIS (6847)
email: orders@ntis.gov <https://www.ntis.gov/about>
Online ordering: http://www.ntis.gov

TRISO Fuel: Properties and Failure Modes

Code Description Document

June 2021

BE Wells
NR Phillips
KJ Geelhood

Pacific Northwest National Laboratory
Richland, Washington 99354

Summary

This report documents the TRISO (TRi-structural ISOtropic) fuel particle properties for FAST (Fuel Analysis under Steady-state and Transients) analysis of TRISO fuel. An overview of the TRISO particle design and production process is provided, and material property data and recommended property selections are presented for each TRISO layer. TRISO particle failure mechanisms are summarized, and model codes that include these mechanisms are listed. Identification of failure limits is made where possible and is specific to the current thermal-mechanical FAST model.

Acronyms and Abbreviations

AGR	Advanced Gas Reactor
BAF	Bacon anisotropy factor
CRP	Coordinated Research Project
FAST	Fuel Analysis under Steady-state and Transients
FIMA	fissions per initial metal atom
HTGR	high-temperature gas-cooled reactor
IPyC	inner pyrolytic carbon
KCMI	kernel-coating mechanical interaction
LEU	low enriched uranium
LWR	light-water reactor
NGNP	Next Generation Nuclear Plant
OPyC	outer pyrolytic carbon
PNNL	Pacific Northwest National Laboratory
SiC	silicon carbide
TRISO	TRi-structural ISOtropic
UCO	uranium oxycarbide

Contents

Figures

Tables

1.0 Introduction

This work was performed under Task Order Number 31310019F0047 for Request for Proposal Modification No. 2 for NRC Agreement Number 31310019N0001. That task order includes two tasks pertinent to this report:

- **Task 8: Perform a Gap Analysis for TRISO Fuel:** The current fuels code was designed to work with the UO_2/zirconium light-water reactor (LWR) fuel system. More recently, new models have been added to support other fuel types due to interest in non-LWR concepts. However, there are no models for TRISO (TRi-structural ISOtropic) fuel behavior in the FAST (Fuel Analysis under Steady-state and Transients) code. This task will focus on what information is available for TRISO fuel behavior and what code updates will be needed to ensure FAST is ready to analyze TRISO fuel. Pacific Northwest National Laboratory (PNNL) shall perform a gap analysis to determine what additional physics and models are necessary to analyze TRISO fuel behavior under steady-state and anticipated transients. The gap analysis shall consider both the behavior within the TRISO particles and in the graphite matrix that binds the particles in a fuel compact. In addition, this review should determine what codes (e.g., PARFUME), data [e.g., Advanced Gas Reactor (AGR) test series], and assessment information are available.

- **Task 9: Document potential TRISO fuel failure modes:** PNNL shall perform a literature survey to determine the potential failure modes for TRISO fuels. Example failure modes include thermal creep and fission product chemical attack. PNNL shall identify limits associated with each failure mode [e.g., fission product concentration limits in the silicon carbide (SiC) layer].

This report documents the approach to fulfill Task 8 and Task 9 and thus provides the TRISO fuel particle properties for FAST analysis of TRISO fuel as described in Geelhood et al. (2021). Section 2.0 provides an overview of the TRISO particle design and production process. Section 3.0 presents material property data and provides recommended property selections. Section 4.0 summarizes the TRISO particle failure mechanisms and lists the codes that include these mechanisms. Identification of failure limits is made where possible and is specific to the current thermal-mechanical FAST model of Geelhood et al. (2021).

2.0 Overview of TRISO Particles

TRISO was invented in the United Kingdom as part of the Dragon reactor project and has been used in many different reactors since. TRISO is currently the fuel form of choice for next generation high-temperature gas-cooled reactors (HTGRs) and very-high-temperature reactors. This latter designation includes pebble bed reactors and prismatic-core reactors (Liu et al. 2020).

The TRISO-coated particle is a spherical, layered composite. The layers that comprise a TRISO particle are the kernel, buffer, inner pyrolytic carbon (IPyC), SiC, and outer pyrolytic carbon (OPyC). Figure 2.1 depicts an HTGR TRISO particle. The layers within the particle work together as a singular containment system, allowing individual particles to retain fission products under nuclear reactor conditions. TRISO particles are typically ~750-830 µm in diameter (Petti et al. 2004) and vary in size based on kernel type and manufacturing process. There are thousands of these TRISO particles that are combined within a carbon matrix to make an individual fuel compact. Fuel compacts come in two different forms: spherical and cylindrical. Spherical fuel compacts, typically called "pebbles," are ~6 cm in diameter and are used in pebble bed type reactors (IAEA 1997). Cylindrical fuel compacts are circular cylinders. U.S. design compacts are 12 mm in diameter and 49 mm long and are used in prismatic reactor types (IAEA 1997).
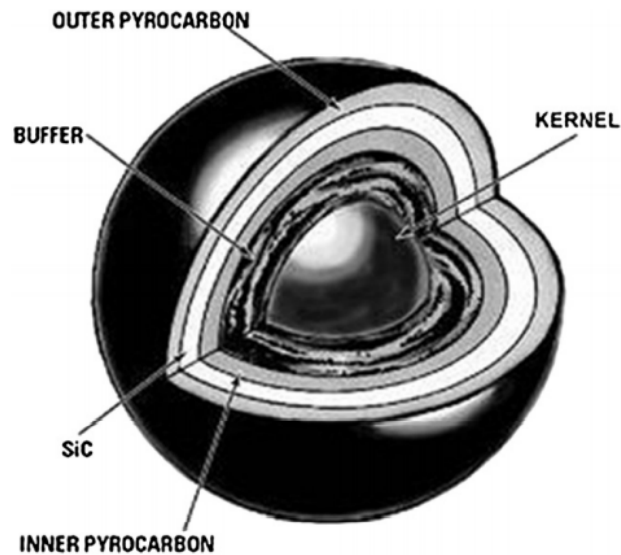
Figure 2.1. HTGR TRISO Coated Fuel Particle (Zhou and Tang 2011)

2.1 Layer Descriptions

The layers of the TRISO particles are briefly described.

2.1.1 Kernel

The kernel is the spherical fissionable fuel at the center of the TRISO particle. In addition to being fissionable fuel, the kernel also serves as a barrier to radionuclide release by immobilizing and/or delaying fission products. A broad range of fissionable fuels are used to make kernels and include: UO_2, $(U,Th)O_2$, UC_2, $(U,Th)C$, PuO_2, and UCO (IAEA 2010). UCO is a conglomerate of UO_2, UC, and UC_2 chemical compounds. The primary difference between the UO_2 and UCO kernels is that the UCO kernels limit oxygen activity. Reducing oxygen activity reduces the generation of CO and CO_2, which has benefits for kernel migration and reducing gas pressure in the particle, allowing for higher burnup limits and thermal gradients.

2.1.2 Buffer

The fuel kernel is surrounded by a porous carbon buffer that attenuates fission recoils and provides void space to accommodate fission gas release. The buffer is low-density, ~50% porous PyC (Liu et al. 2020). The purpose of the buffer is to absorb the kinetic energy of fission fragments ejected from fuel kernel surface and to provide space for the accumulation of gaseous fission products and carbon monoxide. It functions by mechanically decoupling the kernel from the IPyC layer to accommodate kernel swelling. The buffer thickness is 100 μm in U.S. UCO fissile fuel and 65 μm in U.S. UCO fertile fuel (IAEA 1997).

2.1.3 IPyC

The IPyC is a dense layer of carbon with approximately 85% porosity (Marciulescu and Sowder 2019). The IPyC serves several purposes. It protects the kernel from corrosive gases (HCL, CL_2) liberated during the SiC coating process. The IPyC layer is also the first load-bearing barrier and provides structural support for the SiC layer. The IPyC layer also protects the SiC layer from fission products and CO during operation by retaining gaseous fission products (Snead et al. 2007).

2.1.4 SiC

The SiC layer is a high-density, high-strength layer of silicon carbide (Snead et al. 2007). The primary function of the SiC layer is for structural strength of the particle. It provides pressure vessel (refenced to the TRISO particle, not, for example, a reactor vessel) support for internal fission gases and impermeability to metallic fission products.

2.1.5 OPyC

The OPyC is another layer of high-density carbon. The OPyC acts to protect the fuel particle during formation of the fuel compact (Verfondern 2012). The OPyC layer also provides structural support for the SiC layer and acts as additional barrier to the release of gaseous fission products in the event of SiC failure. Because the matrix material of the fuel compact will not bond to the SiC layer, the OPyC layer is necessary to provide a bonding surface between the TRISO particles and the carbonaceous matrix material.

2.1.6   Fuel Compact

The fuel compact is composed of thousands of individual particles that are embedded in a carbonaceous matrix. The purpose of the matrix is to provide a rigid structure, improve heat transfer and temperature uniformity, and retard migration of fission products that are not retained within the TRISO particles (Marciulescu and Sowder 2019). A specific example of the constituents of the matrix are 64% natural graphite, 16% electro-graphite powders, and 20% phenolic resin binder (Tang et al. 2012), other compositions are used.

2.2   Manufacturing Process

The following manufacturing processes for TRISO fuels have been adapted from Morris et al. (2004). The process for UO_2 and UCO particle manufacturing is very similar. Where there are deviations between the two particle manufacturing processes, the following section will remain specific to UCO fuel particles.

2.2.1   Kernel

The kernel is made by an ammonium-based gel-precipitation process. It can be made by either an "internal" or "external" gelation. For internal gelation, a broth is formed when uranium is dissolved in nitric acid and mixed with urea and a carbon. It is then chilled and mixed with hexamethylene (HMTA). Spheres are created when the broth is pulsed through needle orifices, forming droplets that fall into a heated column of immiscible liquid. The spheres sink to the bottom, where they are removed and then washed in ammonium hydroxide to remove ammonium nitrate. The spheres are dried, then calcined and sintered in a hydrogen atmosphere to remove excess oxygen, and then in argon or argon/CO to adjust the O/C ratio. The kernels are screened for size. The external gelation process is similar in nature; however, it instead induces gelation with ammonia external to the droplet. Gelling is accomplished by droplets pulsed through needle orifices through an ammonia vapor phase and into an ammonium hydroxide aqueous column.

2.2.2   Coating Layers

The coating layers are deposited on the kernel in a fluidized bed by thermal cracking of the appropriate gas (e.g., argon). Hydrocarbon gases acetylene and propylene are used for carbon layers. Methyltrichlorosilane is used for SiC layers and it is reduced by hydrogen. Temperatures are in the range of 1200-1500°C and the flow rates of the gases are adjusted to achieve the appropriate deposition rate.

The layer properties are controlled by temperature, coating rate, coating gas composition, bed loading, and particle size. There are two processes for applying the coatings: "continuous" and "interrupted." In the interrupted process, the coater is unloaded after each coating step and particles are checked and sorted for defects, while in the continuous process particles remain in continual process between layer deposition. Trends in manufacturing are leading toward the continual process.

2.2.3   Overcoating

Before the fuel compact is made, often the particles are put through a process of "overcoating," where graphitic matrix material is applied to the exterior of the TRISO particles. The overcoating process starts by placing the particles in a rotating drum. The drum is rotated, and reinstated

graphitic matrix material and solvent are added simultaneously, applying a uniform coating on the particles ~ 200 µm thick. The particles are then dried at 80°C and sieved to select the proper size. The overcoating prevents direct particle-to-particle contact, which may induce cracking of the particle coating layers during compact formation.

2.2.4   Fuel Compacts

There are two different methods for creating fuel compacts: "admix" and "injection." The admix method creates a stronger compact but has a reduced packing fraction (~30-40%), and the injection method has increased packing fraction (~50-60%) but is structurally weaker.

2.2.4.1   Admix

The admix process typically begins with particles that have been overcoated with matrix material. The matrix material for the admix method is a highly viscous mixture of binder and graphite powder. Particles are mixed with matrix material to create a random distribution of particles to a specific volume and placed in a mold. Heat and pressure are used to form the particle mixture together to create the "fueled center" of the compact. An unfueled layer of more matrix material is placed around the "fueled center" and placed into a larger mold where it is formed, resulting in a "green" fuel compact ready for carbonizing. The process allows for ~30-40% packing fraction. Fractions beyond 30-40% have a higher probability of particle breakage.

2.2.4.2   Injection method

The injection method typically begins with overcoated particles. The particles and any shim material are put into a mold and compressed by a piston. A flowable mixture of binder and graphite flour is then injected into the mold, where it is allowed to harden, creating the "green" fuel compact ready for carbonizing. The injected binder may be thermoplastic or thermosetting. A thermoplastic binder cools to harden, and a thermosetting binder hardens at an elevated temperature setpoint. Because the injection method uses a flowable mixture, less filler material is used, allowing for ~50-60% higher packing fractions but making the compact structurally weaker.

2.2.5   Carbonizing

The green fuel compacts are then baked in an inert atmosphere at 800°C to carbonize the binder and vaporize any process additives. Optionally, fuel compacts may be purged with HCl after carbonizing to convert impurities to volatile chlorides that can leave the fuel compact at processing temperatures. The compacts are then baked at 1650-1950°C to further carbonization, improve the crystallinity of the matrix binder, and remove volatile impurities.

3.0   Material Properties of TRISO Particles

Material properties associated with the performance of TRISO particles are provided for the fuel kernel, outer layers, and graphite matrix. Justification for the property selections is presented where available.

3.1   UCO Fuel

Material properties selected to represent the UCO fuel kernel are summarized.

3.1.1   Thermal Conductivity

As described in Section 2.0, UCO fuel kernels can have various compositions of 65-85 mol% UO_2 and 15-35 mol% UCx. Thermal conductivity correlations specific to these compositions for UCO have not been developed. Hales et al. (2020) and Miller et al. (2018) used the thermal conductivity of UO_2, expressed as

$$k = 0.0132e^{0.00188T_C} + \begin{cases} \frac{4040}{464+T_C} \: for \: T_C < 1650 \, °C \\ 1.9 \: for \: T_C \geq 1650 \, °C \end{cases} \tag{3.1}$$

where:
k = thermal conductivity of sphere material (W/m-K)
T_C = temperature of the kernel (°C)

As will be shown, Eq. (3.1) compares favorably with that of Geelhood et al. (2020) for UO_2 at 0% burnup. The Geelhood et al. (2020) model for the thermal conductivity of 95% theoretical density fuel as a function of temperature and burnup is given by

$$k_{95} = \left(\frac{1}{A + \alpha \cdot gad + BT + f(Bu) + (1 - 0.9\exp(-0.04Bu)g(Bu)h(T))} \right) + \frac{C}{T^2} \exp\left(-\frac{D}{T}\right) \tag{3.2}$$

where:
T = temperature (K)
Bu = burnup (GWd/MTU)
$f(Bu)$ = effect of fission products in crystal matrix (solution) = 0.00187*Bu
$g(Bu)$ = effect of irradiation defects = $0.038Bu^{0.28}$
$h(T)$ = temperature dependence of annealing on irradiation defects:

$$h(T) = \frac{1}{1 + 396\exp\left(-\frac{Q}{T}\right)} \tag{3.3}$$

where:
Q = temperature-dependent parameter ("Q/R") = 6380 (K)
A = 0.0452 (m − K/W)
B = 2.46 × 10^{-4} (m − K/W/K)
C = 3.5 × 10^9 (W − K/m)
D = 16361 (K)
α = constant = 1.1599
gad = weight fraction of gadolinia (unitless)

Eq. (3.2) is adjusted for the fuel density (in fraction of theoretical density) as

$$k_d = 1.0789 k_{95} \frac{d}{1 + 0.5(1 - d)} \tag{3.4}$$

where:
k_d = thermal conductivity adjusted for density (W/m-K)
d = traction of fuel theoretical density (unitless)

The effect of using UO_2 thermal conductivity to represent that of UCO, the combination of UO_2 and UCx, is discussed. For UO_2 and UC separately at an example temperature of 25°C, the thermal conductivity UO_2 is 7.6 W/m/K, while that of UC is substantially higher at ~25 W/m/K (Dewi et al. 2020). However, approaches for the effective thermal conductivity of a composite medium, such as the classical model by Maxwell (1873), are not directly applicable to the UCO fuel kernels due to the heterogeneity of the material.

Figure 3.1 presents thermal conductivity as a function of temperature specific to UO_2 and UCO. Representative values for UC thermal conductivity from Bates (1969) with varying oxygen levels, DeConinck et al. (1975) with polycrystalline UC with varying grain size as well as specimens with small fractions of finely dispersed interparticle free U, and Lewis and Kerrisk (1976) of various compositions (including Bates 1969) are shown in relative agreement with each other. The reduced thermal conductivity of UO_2 from Eqs. (3.1) and (3.2) in comparison to that available for UCO materials is shown to agree with that of Ortensi and Ougouag (2009) at 0% burnup. The Geelhood et al. (2020) reduction in thermal conductivity with % burnup is also shown by Ortensi and Ougouag (2009).

With the absence of a thermal conductivity model specific to UCO, and given that lower thermal conductivity is more conservative with respect to thermally driven failure mechanisms for TRISO fuel, the Geelhood et al. (2020) model, Eq. (3.2), is selected for the TRISO UCO. The functional effects on thermal conductivity, e.g., reduced thermal conductivity as burnup increases, are included in the selected model.
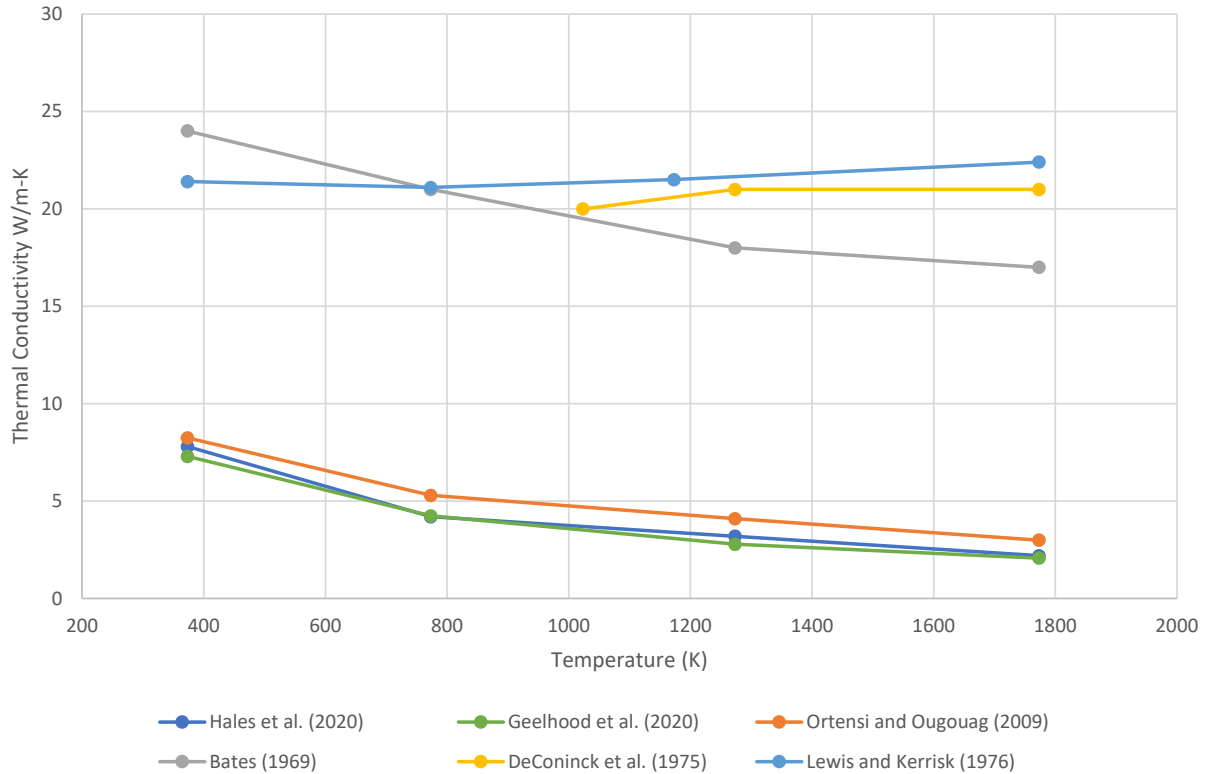
Figure 3.1. Thermal Conductivity of UCO and UO$_2$ as Functions of Temperature

3.1.2   Thermal Expansion

The thermal expansion coefficient specified by Hales et al. (2020) for a UCO kernel is a constant value of 10×10^{-6} (1/K), referenced to Olander (1976). This value is representative of UC data from Chiotti et al. (1966), Men'Shikova et al. (1971), and Richards (1971) over a temperature range up to 2400 K, as shown in Figure 3.2. However, as with the thermal conductivity, the composition of the uranium carbide materials from this literature relative to the UO$_2$ – UCx composition of TRISO UCO fuel kernels is uncertain.

The correlation for UO$_2$ thermal expansion in Geelhood et al. (2020) provides linear strain as a function of temperature:

$$\varepsilon_{th} = K_1 T - K_2 + K_3 \exp\left(-\frac{E_D}{kT}\right) \tag{3.5}$$

where:

ε_{th} = linear strain caused by thermal expansion (293K reference) (unitless)
T = temperature (K)
K_1 = constant, 9.80×10^{-6} (1/K)
K_2 = constant, 2.61×10^{-3} (unitless)
K_3 = constant, 3.16×10^{-1} (unitless)
E_D = energy of formation of a defect, 1.32×10^{-19} (J)
k = Boltzmann's constant = 1.38×10^{-23} (J/K)
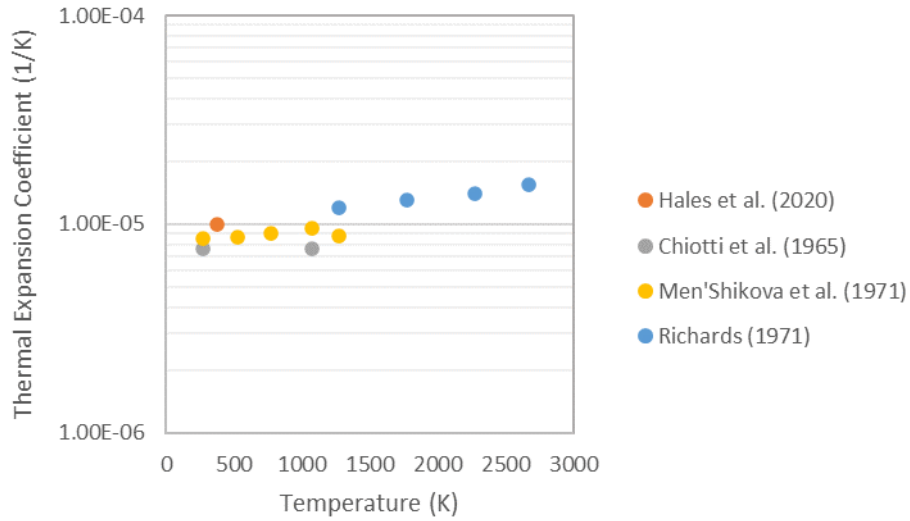
Figure 3.2. Thermal Expansion Coefficients of Uranium Carbide as a Function of Temperature

The linear strain as a function of temperature for the thermal expansion coefficients of UC shown in Figure 3.2 compares favorably with the Geelhood et al. (2020) model, Eq. (3.5), Figure 3.3. At temperatures above approximately 2000 K, the Geelhood et al. (2020) model shows increased linear strain over the Hales et al. (2020) constant thermal expansion coefficient, and is relative agreement with the Richards (1971) UC results. The higher linear strain results in comparison to Hales et al. (2020) are more conservative with respect to thermal failure of TRISO, and the Geelhood et al. (2020) model is selected to represent the TRISO UCO.
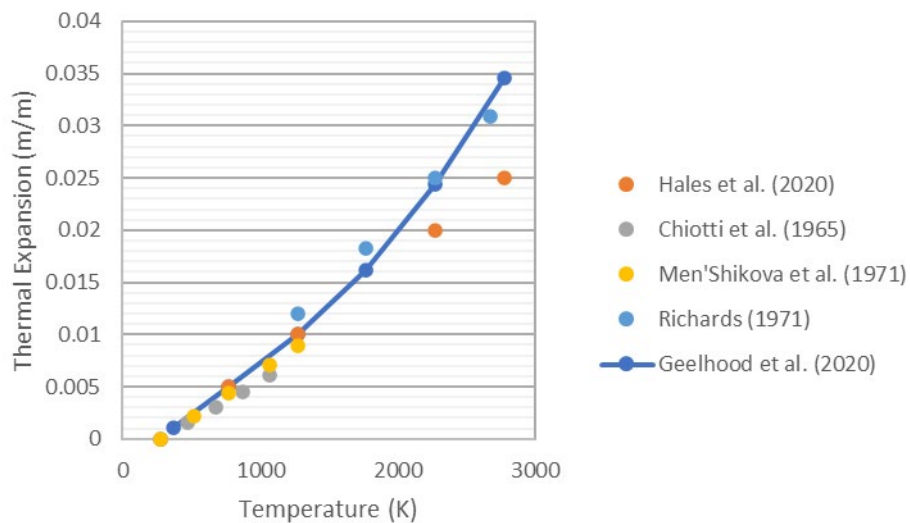
Figure 3.3. Linear Strain of UCO and UO_2 as Functions of Temperature

3.1.3   Melting Temperature

Ma (1983) provides the melting temperature of UC as 2260 K. The melting temperature of UC is given in Ebner (2004) as approximately 2620 K. Depending on the carbon content and structure, Ebner (2004) observes that the melting temperature of UC can vary from approximately 2093 K (body-centered cubic $UC_{1.96}$, melting point denoted as decomposition) to 2670 K (face-centered cubic $UC_{1.86}$). The melting temperature of UO_2 is provided in Geelhood et al. (2020) as a function of burnup as

$$T_{melt} = 3113.15 - 0.5Bu \tag{3.6}$$

where:
T_{melt} = melting temperature (K)
Bu = burnup (GWd/MTU)

Thus, depending on the composition of the UCO fuel kernel and the extent of burnup, a fraction of the UCO fuel may have a lower melting temperature of approximately 2090 K.

3.1.4   Swelling

Hales et al. (2020) noted a "lack of relevant UCO data" and assumed that fission-induced swelling for UO_2 was applicable for UCO. The volumetric swelling was given by

$$\Delta\varepsilon_{SW} = 0.8\Delta Bu \tag{3.7}$$

where:

$\Delta\varepsilon_{SW}$ = volumetric swelling increment
Bu = burnup (fissions per initial metal atom, FIMA)

Geelhood et al. (2020) modeled fuel irradiation swelling in the oxide fuels via two different phenomena; solid swelling and gaseous swelling. Solid swelling proceeds at a constant rate with increasing burnup and with no temperature dependence. Gaseous swelling only occurs at high burnup (>40 GWd/MTU) and occurs over a specific temperature range (1233 to 2105 K).

The solid swelling for UO_2 from Geelhood et al. (2020) is

$$\frac{\Delta V}{V} = \begin{cases} 0 & for\ Bu \leq 6\ GWd/MTU \\ 0.00062(Bu - 6) & for\ 6 < Bu \leq 80\ GWd/MTU \\ 0.00062(74) + 0.00086(Bu - 80) & for\ Bu > 80\ GWd/MTU \end{cases} \tag{3.8}$$

where:
$\Delta V/V$ = fuel volumetric swelling (unitless)
Bu = burnup (GWd/MTU)

At burnup levels greater than approximately 200 GWd/MTU, close agreement is shown for Eqs. (3.7) and (3.8), Figure 3.4 (a conversion of 1% FIMA = 9.6 GWd/t(HM) was used, e.g., Devida et al. 2004).
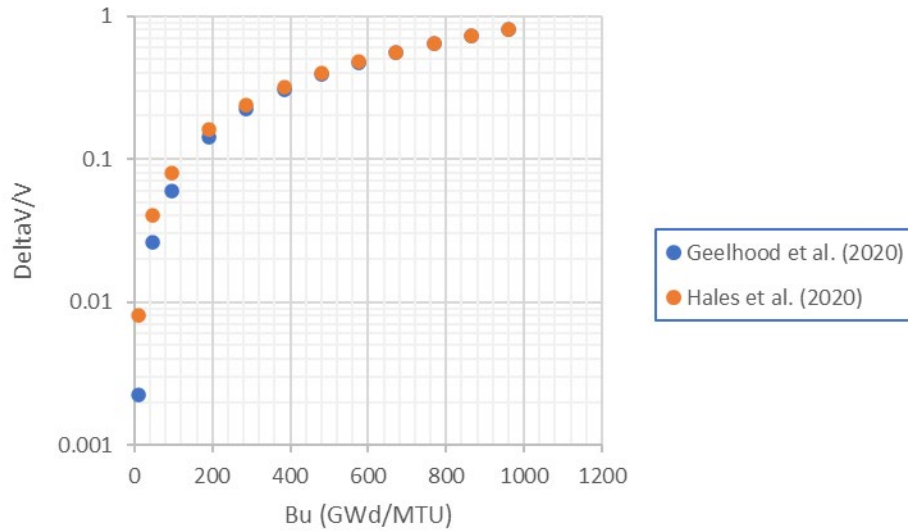
Figure 3.4. UO$_2$ Volumetric Swelling as a Function of Burnup

Volumetric swelling is related to linear swelling by

$$\frac{\Delta L}{L} = \left(1 + \frac{\Delta V}{V}\right)^{\frac{1}{3}} - 1 \qquad (3.9)$$

where:
$\Delta L/L$ = fuel linear swelling (unitless)

The Geelhood et al. (2020) expression for the gaseous swelling of UO$_2$ is given as functions of burnup and temperature:

For Bu ≤ 40 GWd/MTU:

$$\frac{\Delta L}{L} = 0 \qquad (3.10)$$

40 < Bu < 50 GWd/MTU:

$$\frac{\Delta L}{L} = \begin{cases} 0 & for\ T < 1233\ K \\ \frac{Bu-40}{10}(-4.37E-2+4.55E-5T) & for\ 1233 \leq T < 1643\ K \\ \frac{Bu-40}{10}(7.40E-2-4.05E-5T) & for\ 1643 \leq T < 2105\ K \\ 0 & for\ T > 2105\ K \end{cases} \qquad (3.11)$$

Bu ≥ 50 GWd/MTU:

$$\frac{\Delta L}{L} = \begin{cases} 0 & for\ T < 1233\ K \\ -4.37E-2+4.55E-5T & for\ 1233 \leq T < 1643\ K \\ 7.40E-2-4.05E-5T & for\ 1643 \leq T < 2105\ K \\ 0 & for\ T > 2105\ K \end{cases} \qquad (3.12)$$

3.1.5   Density

The density of UCO varies depending on the composition and production process. Nagley et al. (2010) provide characterizations of the UCO kernels produced for the AGR fuel tests at Idaho National Laboratory, and reported mean density values of 10.7 to 11.0 g/mL, depending on production lot as shown in Table 3.1.

Jolly et al. (2015) reported a density of 10.92 g/mL for the AGR-1 kernels. McMurray et al. (2017) used a density range of 10.65 to 10.85 g/mL, within the UCO densities of Table 3.1, to develop general oxygen balance formulas for calculating the minimum UCx content to ensure negligible CO formation of UCO taken to a specific burnup.

Table 3.1. UCO Density and Standard Deviation from Nagley et al. (2010)

Kernel Lot	UCO Mean Density (g/mL)	UCO Standard Deviation (g/mL)	~99% Confidence Interval Density Range[a] (g/mL)
AGR-1	10.7	0.026	10.62 – 10.78
AGR-2	11.0	0.030	10.91 – 11.09
AGR-3 and 4	10.9	0.030	10.81 – 10.99
Lot 69311	10.8	0.023	10.73 – 10.87

(a) Computed from three standard deviations with assumption of normal distribution.

Hales et al. (2020) provide a methodology to compute the theoretical density of UCO based on its composition. Hales et al. (2020) assumed that UCO is solely formed of UO_2, UC_2, and UC for the density calculation but note that, as described in Section 2.0 of this report, UC_2 and UC are known to mix during the heat treatment process and form a UCx phase where x < 2. With the assumption of UO_2, UC_2, and UC, the theoretical density of the kernel can be calculated from

$$\rho_{th} = \frac{1}{\frac{wf_{UO_2}}{\rho_{th}^{UO_2}} + \frac{wf_{UC}}{\rho_{th}^{UC}} + \frac{wf_{UC_2}}{\rho_{th}^{UC_2}}} \tag{3.13}$$

and

$$wf = \frac{af \times aw}{M} \tag{3.14}$$

where:
wf = weight fraction of denoted constituent
ρ_{th} = theoretical density of denoted constituent
M = molar mass

$$M = \sum_{i}^{N} af_i \times aw_i \qquad (3.15)$$

where:
i = UO$_2$, UC$_2$, and UC
af = atomic fraction
aw = atomic weight (kg/mol)

$$af = \begin{cases} 0.5OU \ for \ UO_2 \\ 0.5OU + CU - 1.0 \ for \ UC_2 \\ 2.0 - (OU + CU) \ for \ UC \end{cases} \qquad (3.16)$$

where:
OU = oxygen to uranium ratio of UCO
CU = carbon to uranium ratio of UCO

$$aw = \begin{cases} 0.23504\varepsilon + 0.23805(1.0 - \varepsilon) + 0.03200 \ for \ UO_2 \\ 0.23504\varepsilon + 0.23805(1.0 - \varepsilon) + 0.02402 \ for \ UC_2 \\ 0.23504\varepsilon + 0.23805(1.0 - \varepsilon) + 0.01201 \ for \ UC \end{cases} \qquad (3.17)$$

where:
ε = initial U-235 enrichment (wt%)

Hales et al. (2020) list the constituent phase densities as given in Table 3.2. In application, the compositional ranges, including initial enrichment, vary as described in Section 2.0. Calculation of theoretical density values from Eqs. (3.13) through(3.17) using the oxygen to uranium and carbon to uranium ratios and initial enrichment values reported in Nagley et al. (2010) (UC$_2$ assumed) yields densities greater than those of Table 3.1 at approximately 11.26 g/mL.

Table 3.2. Theoretical Density Values (Hales et al. 2020)

	UO$_2$	UC	UC$_2$
Density (g/mL)	10.96	13.63	11.28

3.2 Buffer Carbon

Buffer carbon material properties are summarized.

3.2.1 Thermal Conductivity

The thermal conductivity of the buffer carbon is given by Hales et al. (2020) as a function of the layer density as

$$k = \frac{k_i k_t \rho_t (\rho_t - \rho_i)}{k_t \rho_t (\rho_t - \rho) + k_i \rho (\rho - \rho_i)} \tag{3.18}$$

where:
i = initial value
t = theoretical value
k = thermal conductivity (W/m-K)
ρ = density (kg/m^3)

The initial and theoretical thermal conductivities are specified as 0.5 and 4 W/m-K, respectively.

The thermal conductivity of the buffer carbon is given as a function of porosity by Petti et al. (2004) as

$$k = 10.98222 \left(\frac{1-P}{1+2P} \right) + 0.00444 \tag{3.19}$$

where:
P = fractional porosity
k = thermal conductivity (W/m-K)

With the fractional porosity defined by P = 1-(ρ/ρ_t), and ρ_i = 1.05 g/mL and ρ_t = 2.2 g/mL (see Section 3.2.4), the initial porosity is approximately 0.52. For comparison, Liu et al. (2020) and Verfondern (2012) state the buffer layer is ~50% porous of the theoretical density 2.2 g/mL. The results of the Petti et al. (2004) model, Eq. (3.18), are shown to be substantially larger than those of Hales et al. (2020), Eq. (3.18) (Figure 3.5).

Wei et al. (2019) developed and verified a theoretical model using finite element analysis for the effective thermal conductivity of porous carbon during irradiation, where the porosity, the moles of released gases in the pores, and the pore pressure are considered to evolve with burnup. Over a porosity range of 0% to 50%, the effective thermal conductivity of the buffer layer decreases from approximately 4 to 1.5 W/m-K, in relative agreement with the Hales et al. (2020) model.

Powers and Wirth (2010) note that the correlation they present "yields significantly higher thermal conductivities for the PyC buffer layer" than other correlations recommended, and "since the magnitude of the temperature gradient across a TRISO fuel particle is almost entirely determined by the temperature drop across the buffer layer, this could have a large impact on fuel performance calculations." Given the similarity of the Hales et al (2020) model results with those of Wei et al. (2019) as well as the more-dense PyC layers (Section 3.3.1), the Hales et al. (2020) model is selected to represent the TRISO buffer carbon.
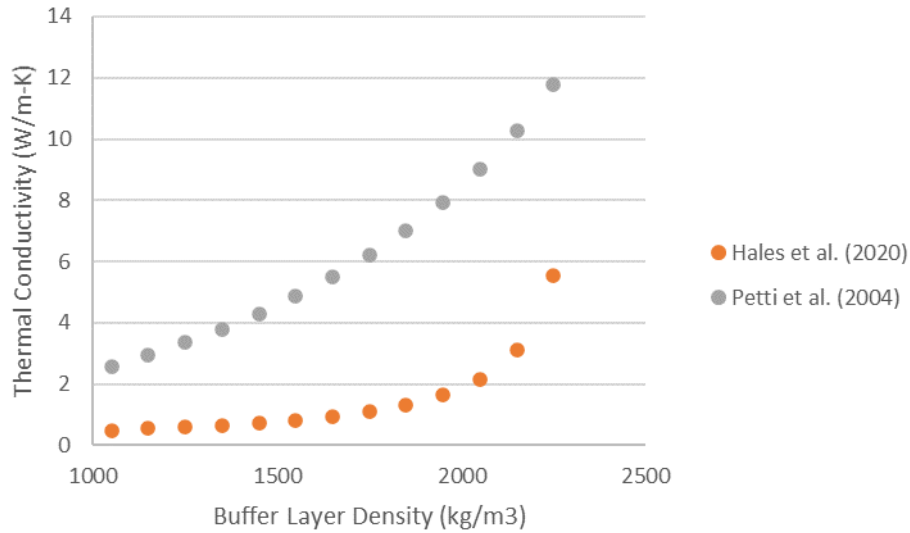
Figure 3.5. Buffer Carbon Thermal Conductivity as a Function of Density

3.2.2   Thermal Expansion

Hales et al. (2020) specify that the thermal expansion coefficient of the buffer carbon can be express as a function of its temperature as

$$\alpha = 5\left(1 + 0.11\frac{T_C - 400}{700}\right)$$

(3.20)

where:
α = thermal expansion coefficient (10^{-6}/K)
T_C = temperature of the buffer carbon (°C)

This expression of the thermal expansion coefficient results from the isotropic behavior of the buffer carbon (Miller et al. 2018), as given by the expressions for the thermal expansion coefficient of the PyC in the radial and tangential directions provided in Section 3.3.2, with R_r = R_t = R = 2/3. (R is the orientation parameter, and the subscripts r and t denote the radial and tangential directions respectively, see Section 3.3.2.)

The linear strain as a function of temperature for the thermal expansion coefficient of Eq. (3.20) with the strain at 293 K = 0 is expressed as

$$\varepsilon_{th} = 3.92857 \times 10^{-10}T_C^2 + 4.4711 \times 10^{-6}T_C - 1.343758 \times 10^{-3}$$

(3.21)

where:
ε_{th} = linear strain caused by thermal expansion (293 K reference) (unitless)
T_C = temperature of the buffer carbon (K)

3.2.3   Melting Temperature

The melting temperature of the buffer carbon set to the constant value of 3800 K, equivalent to the pyrolytic carbon melting temperature selected from Savvatimskiy (2003), Section 3.3.3.

3.2.4   Density

Density ranges for the buffer carbon are provided in numerous references. Characterizations of TRISO particles produced for the AGR fuel tests are summarized in Marciulescu and Sowder (2019), who refer to the buffer layer as "low-density (~50% of theoretical), porous PyC buffer coating." The buffer layer density from TRISO particle characterization is approximately 1.1 g/mL for AGR-1 tests and approximately 1.04 and 0.99 g/mL for AGR-2 tests with UCO and UO_2 kernels, respectively. Specifications for the mean density ranges for acceptable fuel performance are provided as 0.88 to 1.18 g/mL and 0.95 to 1.15 g/mL for AGR-1 and AGR-2, respectively. A typical density value is thus approximately 1.05 g/mL.

Similar values for buffer layer density are listed for other fuels. IAEA (1997) provides a specification of ≤ 1.1 g/mL for the HTR-10 fuel element. UO_2 kernel fuel particles irradiated in the Russian IVV-2M reactor had buffer layer densities of 1.02 and 1.05 g/mL (Petti et al. 2012).

With respect to the Marciulescu and Sowder (2019) denotation of ~50% of theoretical density, Petti et al. (2004) list the theoretical density of graphite material as 2.27 g/mL, and the theoretical density of PyC as 2.2 g/mL. Petti et al. (2004) used similar values with the as-fabricated density range of the buffer layer as 0.9 to 1.1 g/mL.

3.3   Pyrolytic Carbon

Material properties selected for the PyC layer are summarized.

3.3.1   Thermal Conductivity

López-Honorato et al. (2008) mapped the thermal conductivity of PyC coatings on spherical particles using time-domain thermoreflectance. The results show small variations across the coating layers and indicate uniformity of the coatings, and range between 3.4 and 13.5 W/m-K for PyC coatings with different densities and microstructures. The observed differences were not explained by changes in total porosity alone, and porosity – together with anisotropy, structural disorder, and domain size – appears to affect the thermal conductivity of PyC. With a similar maximum, Wang et al. (2018) determined radial and circumferential thermal conductivities of 0.28 and 11.5 W/m-K, respectively, for a PyC layer using a laser-based thermoreflectance technique. Wang et al. (2018) hypothesized that porosity and debonding between graphitic planes are responsible for additional reduction in thermal conductivity in the radial direction beyond the theoretical minimum limit of graphite's cross-plane conductivity.

As described for the UCO kernel (Section 3.1.1), lower thermal conductivity is more conservative with respect to thermally driven failure mechanisms for TRISO fuel. Hales et al. (2020) selected 4 W/m-K, which is representative of the lower range of the López-Honorato et al. (2008) results. A constant value of 4 W/m-K is selected for the pyrolytic carbon thermal conductivity.

3.3.2   Thermal Expansion

The thermal expansion of PyC has been shown to primarily depend on the degree of preferred orientation of the crystallites and internal accommodations that result from porosity (Ho 1993). Ho (1993) notes further that studies have shown significant differences in the thermal expansion coefficient in the radial and tangential directions.

Ho (1993) describes this anisotropy of the thermal expansion by a Bacon anisotropy factor (BAF). Miller et al. (2018) add a temperature adjustment factor to the PyC thermal expansion coefficients α (10^{-6}/°C) of Ho (1993) as

$$\alpha_r = A(-37.5R_r + 30) \qquad (3.22)$$

and

$$\alpha_t = A(36R_t - 1)^2 + 1 \qquad (3.23)$$

where:
r = radial direction
t = tangential direction
R = orientation parameter, given by

$$R_r = 2/(2 + BAF) \qquad (3.24)$$

$$R_t = 1 - R_r/2 \qquad (3.25)$$

A = temperature adjustment factor, given by

$$A = 1 + 0.11(T - 400)/700 \qquad (3.26)$$

T = temperature of the PyC layer (°C)

For dense PyC, Ho (1993) provides BAF typical values of 1.05 ± 0.05. With BAF = 1.05, conversion of Eqs. (3.22) and (3.23) to linear strain as a function of temperature yields

$$\varepsilon_r = \left(7.85714 \times 10^{-11}T_K{}^2 + 8.94243 \times 10^{-7}T_K - 2.68758 \times 10^{-4}\right)r \qquad (3.27)$$

and

$$\varepsilon_t = (7.85714 \times 10^{-11}T_K T^2 + 8.94243 \times 10^{-7}T_K - 2.68758 \times 10^{-4})t \qquad (3.28)$$

where:
ε = linear strain caused by thermal expansion (293K reference) (unitless)
T_K = temperature of the PyC layer (K)

and

$$r = -37.5 \left[\frac{2}{2 + BAF} \right] + 30 \tag{3.29}$$

$$t = 36 \left[\frac{BAF}{2} - 1 \right]^2 + 1 \tag{3.30}$$

3.3.3   Melting Temperature

Information specific to the melting temperature of PyC in the TRISO application was not identified. However, Savvatimskiy (2003) provides an extensive review of experimental data and theoretical predictions on the melting point of graphite and carbon. Savvatimskiy (2003) noted that the experimental results indicate that the true melting temperature of graphite is in the range of 4000 or 5000 K, and that numerous investigations of graphite involved the recording of high melting points of graphite (4530 to 5080 K). The steady-state value of pressure at the triple point was referenced to be above 10 MPa. Savvatimskiy (2003) further reported on an interpretation of the parameters for the triple point of carbon at a pressure of 0.1 MPa and temperature of 3800 K. This latter value is in relative agreement with vendor specifications for the melting point of pyrolytic graphite, e.g., 3793 to 3923 K.[1] A constant value of 3800 K is recommended for the melting temperature of the PyC layers.

3.3.4   Swelling

Ho (1993) describes that when PyC is irradiated with fast neutrons, energetic knock-on carbon atoms are generated by the collision of the neutrons with the carbon atoms in the lattice. The displaced carbon atoms and produced vacancies can recombine, nucleate to form loops, or are annihilated at structural defects. The competition for these defects results in structure-sensitive dimensional changes that vary in a complicated way with temperature, and as a direct result, the bulk dimensions of the PyC also change. The anisotropic PyC shrinks in the parallel direction, a behavior that reverses at very large fluences, and also initially shrinks in the perpendicular direction but reverses to rapid expansion at low fluence.

IAEA (2010) assumes a constant, isotropic swelling rate of $\Delta L/L$ = -0.005 (/10^{25} n/m^2, E>0.18). Miller et al. (2018) describe the anisotropic PyC swelling as a function of fluence level, PyC density, degree of anisotropy, and irradiation temperature. PyC layer swelling is not currently incorporated into Geelhood et al. (2021).

3.3.5   Density

Pyrolytic carbon density values range from 1.8 to 2.0 g/mL. Marciulescu and Sowder (2019) list the specifications for the mean density ranges for acceptable fuel performance for the inner and outer PyC layers as 1.85 to 1.95 g/mL. From TRISO particle characterization, Marciulescu and Sowder (2019) report 1.853 to 1.912 g/mL for AGR-1 tests, and 1.89 to 1.907 g/mL and 1.884 to approximately 1.89 g/mL for AGR-2 tests with UCO and UO$_2$ kernels, respectively. Values of 1.86 to 1.9 g/mL are provided in IAEA (1997). Petti et al. (2004) specify the as-fabricated

---

[1] https://special-metals.co.uk/materials/pyrolytic-graphite/

density range of the PyC layers as 1.8 to 2 g/mL, and Miller et al. (2018) list the same density range. A density of 1.9 g/mL is recommended for the PyC layers.

3.3.6   Elastic Modulus and Poisson's Ratio

Ho (1993) developed expressions for the elastic moduli of PyC as functions of the layer density, degree of anisotropy (as measured by BAF), apparent crystallite size, fast fluence, and temperature. The elastic modulus in the radial direction is given by

$$E_r = E_{0r}(0.384 + 0.324\rho)(1.463 + 0.463BAF_0)(2.985 - 0.0662L_c)(1 + 0.23\varphi)(1 + 0.00015T) \quad (3.31)$$

and in the tangential direction by

$$E_t = E_{0t}(0.384 + 0.324\rho)(0.481 + 0.519BAF_0)(2.985 - 0.0662L_c)(1 + 0.23\varphi)(1 + 0.00015T) \quad (3.32)$$

for BAF ≤ 2.15, where:
E_0 = refence value at reference ρ (25.5 GPa, Ho 1993)
ρ = layer density (1.9 g/mL, see Section 3.3.4)
L_c = crystallite diameter size (30 angstroms, Ho 1993)
BAF_0 = initial degree of anisotropy (1.05, see Section 3.3.2)
φ = fluence ($\varphi \le 4 \times 10^{21}$ n/m^2, Ho 1993 (in units of nvt))
T = layer temperature (°C)

Figure 3.6 shows example results for Eqs. (3.31) and (3.32) at 20°C and 2000°C as a function of fluence. These results compare reasonably well with those shown in Petti et al. (2004) for the same expressions, but Miller et al. (2018) use these same expressions with 45 angstroms for the crystallite diameter size, which results in values that are reduced by approximately two orders of magnitude. Also shown in Figure 3.6 are results for other fuels from Petti et al. (2004), which they denote as "German" and "UK," and a relatively favorable comparison is shown to the Ho (1993) results. Similarly, measurements taken on cross sections of inner and outer PyC layers yielded elastic moduli of 18 and 23 GPa, respectively (IAEA 2010). Given the effect and uncertainty of the variables for the Ho (1993) model, a fixed value of 25.5 GPa is selected for the PyC layers.
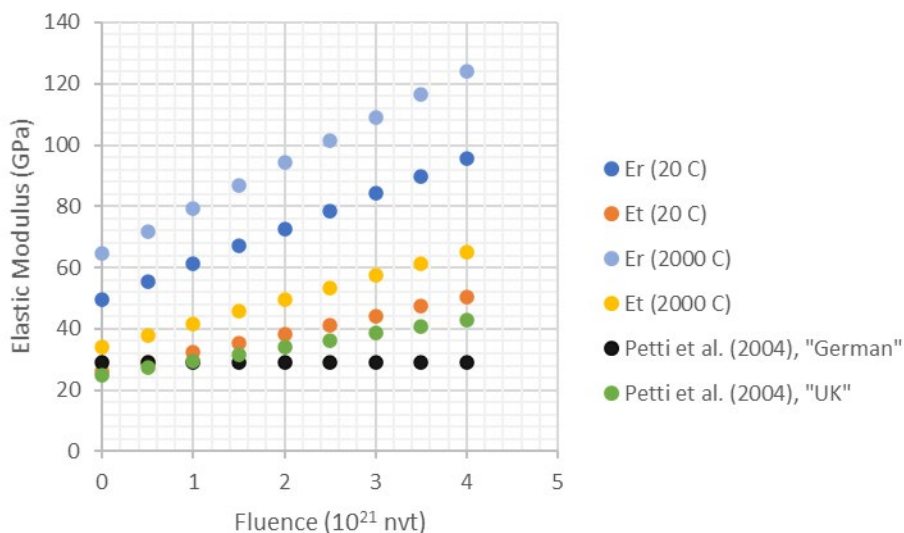
Figure 3.6. Elastic Modulus of PyC as a Function of Fluence

Ho (1993) noted that the dependence of Poisson's ratio on the parameters of Eqs. (3.31) and (3.32) was largely unknown, assumed that it was independent of those parameters, and developed anisotropic expressions for Poisson's ratio fit to limited data as a function of the preferred orientation parameter. For an isotropic material with the preferred orientation parameter set to 2/3 (see Section 3.2.2), a Poisson's ratio of approximately 0.23 is achieved, in relative agreement with the Petti et al. (2004) value for "UK" fuel, 0.21. Miller et al. (2018) specify a larger Poisson's ratio of 0.33, which is also reported by Kovacs et al. (1985) and Li et al. (2019), and is the value applied by IAEA (2012) for benchmark calculations with fuel performance models. A constant value of 0.33 is recommended for the PyC Poisson's ratio.

3.3.7 Strength and Weibull Modulus

Weibull strength parameters were determined for PyC from three-point bend strength test data (Ho 1993). The Weibull modulus was found to be independent of the coating rate and weakly dependent on the PyC density. Although correlations with density were presented, Ho (1993) recommended a constant Weibull modulus value of 9.5 for both the inner and outer PyC layers. This value for the Weibull modulus corresponds to the irradiated value specified in IAEA (2012). [A Weibull modulus of 5 is specified therein for unirradiated PyC; Kovacs et al. (1985) lists a Weibull modulus of 4.]

Ho (1993) provides the characteristic strength of PyC as functions of the layer density, degree of anisotropy (as measured by BAF), fluence, and temperature, and assumed isotropic behavior. For the density range of the PyC layers, 1.8 to 2.0 g/mL (Section 3.3.5), the data presented in Ho (1993) indicates a constant fracture strength value of approximately 75E3 psi (~518 MPa) for near isotropic carbons with BAF < 1.1 (BAF PyC ~ 1.05, Ho 1993).[1] A fracture

---

[1] The "fracture strength" value, units MPa, is related to the "characteristic strength", units MPa $\mu m^{3/m}$, in Ho (1993) by a factor of $[V/2(m + 1)^2]^{1/m}$, where V is the specimen volume between two outer supports in a three-point bend test. Ho (1993) notes that the characteristic strength differs from specimen group to specimen group due to differences in Weibull modulus (m) values, negating statical analysis of the results. IAEA (2012) provides an expression for the probability of failure of single spherical coating layer

strength value of approximately 35E3 psi (~241 MPa) is indicated at a density of ~1.42 g/mL. This latter value is much closer in magnitude to that used in IAEA (2012) for irradiated PyC, 218 MPa (m = 9.5), than the substantially higher value reported for higher PyC densities. 200 MPa is specified for unirradiated PyC by IAEA (2012) with m = 5 (see also Powers 2011). For density 1.9 g/mL and BAF ~ 1.04, Ho (1993) also reports a strength of 384 MPa. Due to the lack of test data, Ho (1993) provides discussion justifying the assumption that strength in the perpendicular direction is the same as that in the parallel direction for the purpose of evaluation of the probability of incipient failure.

For conservatism and to represent an irradiated condition, a constant value of 218 MPa is recommended for PyC mean failure stress with a corresponding value of 9.5 for the Weibull modulus.

3.4 Silicon Carbide

The SiC layer material properties are summarized.

3.4.1 Thermal Conductivity

Snead et al. (2007) report that the thermal conductivity of SiC has been investigated over a wide temperature range of ~ 100 to 1800 K. Figure 3.7 shows the temperature dependence of the thermal conductivity of β-SiC over this temperature range, noted by Snead et al. (2007) to accurately describe the thermal conductivity of a TRISO SiC layer. As summarized in Snead et al. (2007), below 200 K, the thermal conductivity of SiC increases rapidly with increasing temperature due to the large contribution from the specific heat. At temperatures above the peak in thermal conductivity at approximately 200 K, the thermal conductivity decreases significantly with increasing temperature due primarily to the phonon–phonon scattering.

The thermal conductivity of SiC also depends on the nature of grain boundaries and, as shown in Figure 3.7, the magnitude of the thermal conductivity of SiC depends on the grains size. Thermal conductivity monotonically increases with grain size, but the effect of grain size becomes less important with increasing temperature (Snead et al. 2007).

Neutron irradiation rapidly reduces the thermal conductivity of SiC. Senor et al. (1996), Ho (1993), and Hollenberg et al. (1993) provide data that show the thermal conductivity of irradiated SiC is reduced and relatively temperature independent after irradiation. Senor et al. (1996) postulated that the reduced thermal conductivity is caused by the presence of irradiation-induced defects, and noted that annealing the irradiated specimens produced an increase in thermal conductivity. However, multiple post-irradiation anneals on CVD β-SiC indicated that a portion of the irradiation-induced damage was permanent.

---

with a "Weibull equation" that compares the maximum stress in a layer to the median strength of that layer with both terms in units of Pa. To enable the direct use of that expression, and in the absence of specimen volumes, only literature with fracture strength (Ho 1993), "mean strength" (IAEA 2012), and "Weibull mean strength" (Powers 2011) are reported herein, and the results are assumed to be representative of the median strength term for IAEA (2012). For additional values of the characteristic strength in units of MPa m$^{3/m}$, see, for example, Miller et al. (2018). It is also noted that Snead et al. (2007) reference "characteristic strength" with units of MPa.

The upper limit of the thermal conductivity of SiC from Figure 3.7 [denoted as Equation (12) in Figure 3.7] is specified in Snead et al. (2007) as

$$k = \frac{1}{-0.0003 + 1.05 \times 10^{-5}T} \tag{3.33}$$

where:
T = SiC layer temperature (K)

This expression, together with the thermal conductivity data of irradiated SiC from Ho (1993), are shown in Figure 3.8. Also shown in Figure 3.8 is the SiC thermal conductivity as a function of layer temperature from Miller et al. (2018), as

$$k = \frac{17,885}{T} + 2 \tag{3.34}$$

Based on the agreement of the Miller et al. (2018) model with the Ho (1993) data, as well as the conservatism of lower thermal conductivity for thermally driven failure mechanisms for TRISO fuel, Eq. (3.34) is selected for the thermal conductivity of SiC as a function of temperature.

Legend	Reference	Material	Note
◆	Taylor et al [46]	N/R	Single Crystal
▲	Rohm and Haas Co. [32]	CVD	Grain size ~5μm
■	Senor et al. [47]	CVD	Morton CVD
●	Graebner et al. [48]	CVD	Morton CVD
◇	Pickering et al. [33]	CVD	Grain size ~10μm
△	Rohde [49]	CVD	Grain size ~3μm
□	Collins et al. [34]	CVD	Grain size >10μm
○	Collins et al. [34]	CVD	Grain size <10μm
+	Price [50]	FB	Grain size <5μm
×	Price [51]	FB	Grain size <5μm
*	Shaffer [30]	PS	
◎	Li et al. [52]	-	Calculated value

PS: pressureless sintered, HP: hot-pressed
CVD: chemically vapor deposited, FB: fluidized bed
N/R: not reported

Figure 3.7. Thermal Conductivity of SiC as a Function of Temperature and Grain Size (from Snead et al. 2007, specified references listed therein)
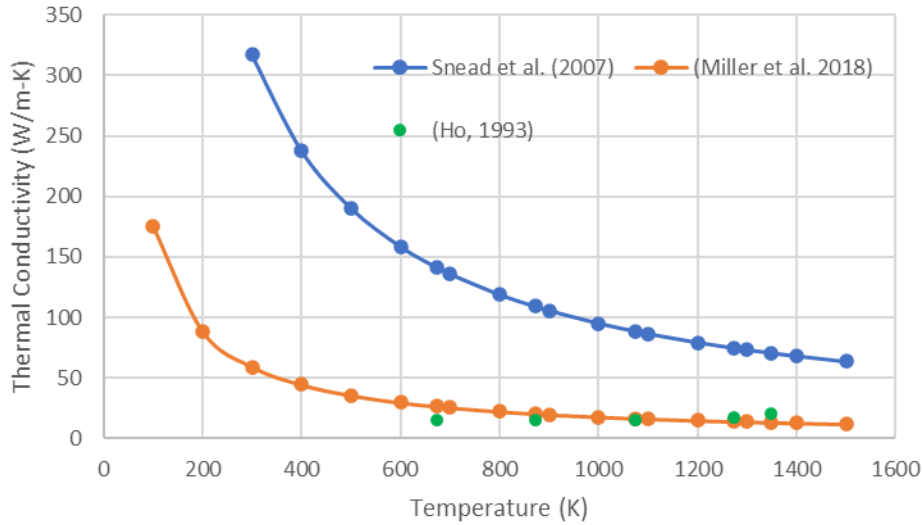
Figure 3.8. Thermal Conductivity of SiC

3.4.2   Thermal Expansion

The coefficient of thermal expansion for SiC has been reported over a wide temperature range (Snead et al. 2007). As shown in Figure 3.9, Snead et al. (2007) developed two expressions for the thermal expansion coefficient. For the expression denoted as "Equation 16" in Figure 3.9 over the temperature range of 125 ≤ T ≤ 1273 K, the thermal expansion coefficient is described as a function of temperature by

$$\alpha = -1.8276 + 0.0178T - 1.5544 \times 10^{-5}T^2 + 4.5246 \times 10^{-9}T^3 \tag{3.35}$$

where:
α = thermal expansion coefficient (10^{-6}/K)
T = SiC layer temperature (K)

Above 1273 K, Snead et al. (2007) assume the thermal expansion coefficient is constant at 5.0 10^{-6}/K. Converting to linear strain at a reference temperature of 293 K yields

$$\varepsilon_{th} = 1.13115 \times 10^{-15}T^4 - 5.18133 \times 10^{-12}T^3 + 8.9 \times 10^{-9}T^2 - 1.8276 \times 10^{-6}T - 1.06575 \times 10^{-4} \tag{3.36}$$

for 125 ≤ T ≤ 1273 K, and

$$\varepsilon_{th} = 5 \times 10^{-6}T - 2.09362 \times 10^{-3} \tag{3.37}$$

for T > 1273 K, where:
ε_{th} = linear strain caused by thermal expansion (unitless)
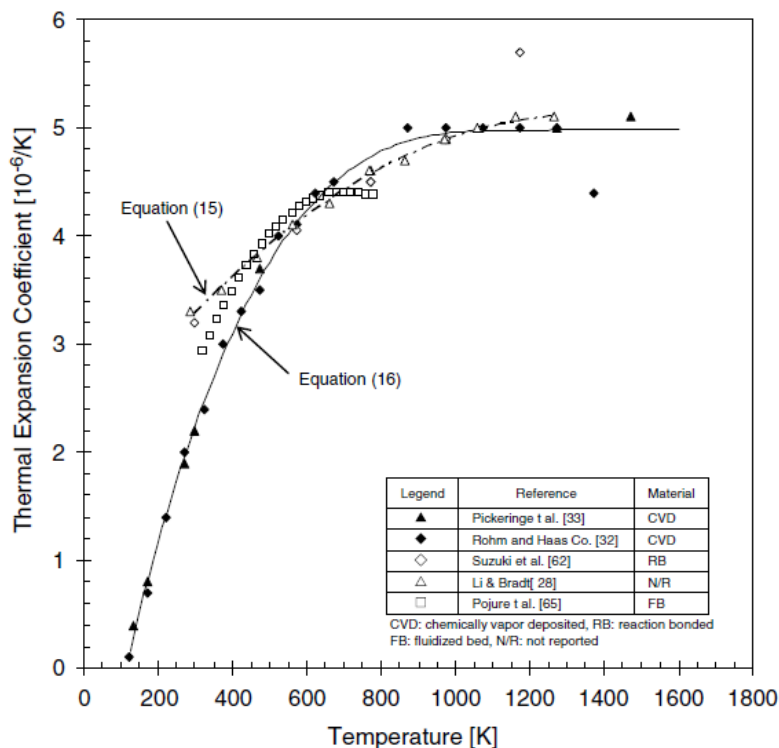
Figure 3.9. Coefficient of Thermal Expansion of SiC as a Function of Temperature (from Snead et al. 2007, specified references listed therein)

3.4.3 Melting Temperature

Haynes (2011) provides the melting temperature of SiC as 3103 K. However, as discussed in Petti et al. (2004), SiC begins to thermally decompose above 2273 K. Petti et al. (2004) note that the SiC thermal decomposition becomes a significant fuel failure mechanism at temperatures generally above 1873 K.

Snead et al. (2017) report that several studies have reported conflicting decomposition temperatures and species for SiC, and that the most reliable thermal decomposition temperature of SiC is 2818 K. This temperature is above the thermal decomposition rate data presented in Petti et al. (2004), which ranges from approximately 2170 K to 2440 K (with corresponding thermal decomposition rates of approximately 1E-10 to 1E-9 m/s). Petti et al. (2004) note that, since SiC that is covered by a layer of pyrolytic carbon, it decomposes more slowly than exposed SiC, and thus the decomposition rate data may be considered to be conservative.

As discussed in Section 4.2, Zhou and Tang (2011) concluded that temperatures that are kept higher than 1600°C (1873 K) for an extended duration can lead to high fuel failure rates, and failures started above approximately 1800°C (2073 K). The temperature of interest selected for SiC thermal decomposition is 1873 K.

3.4.4 Swelling

Snead et al. (2007) describe the irradiation-induced swelling of SiC as having an amorphization regime (<423 K), a saturatable point-defect swelling regime (423-1073 K), and a non-saturated void-swelling regime that occurs for irradiation temperatures >1273 K, although the actual transition temperature for this last regime is unclear. Snead et al. further note that it is unclear how swelling will increase as a function of dose above 10 dpa.

Miller et al. (2018) treat irradiation swelling as negligible in accordance with the recommendation of Ho (1993). SiC layer swelling is not currently incorporated into Geelhood et al. (2021).

3.4.5 Density

Snead et al. (2017) report the density value of high-purity unirradiated SiC as 3.21 g/mL. Marciulescu and Sowder (2019) list the specification for the mean density range for acceptable fuel performance for the SiC layer as ≥ 3.19 g/mL, and from TRISO particle characterization approximately 3.21 g/mL for AGR-1 tests, and 3.197 and 3.2 g/mL for AGR-2 tests with UCO and UO_2 kernels, respectively. Values of 3.18 to 3.21 g/mL are provided in IAEA (1997). Petti et al. (2004) assume an SiC density value of 3.2 g/mL, and Miller et al. (2018) a density of ≥ 3.18 g/mL. A density of 3.2 g/mL is selected for the unirradiated SiC layer.

3.4.6 Elastic Modulus and Poisson's Ratio

Ho (1993) notes that there is relatively large variability in the elastic modulus of SiC. Miller et al. (2018) use the linear interpolation of the Ho (1993) elastic modulus data points as shown in Figure 3.10. Figure 3.10 also shows the functionality with temperature provided in Snead et al. (2017) as

$$E = 460 - 0.04Te^{\left(\frac{962}{T}\right)} \tag{3.38}$$

where:
E = elastic modulus (GPa)
T = SiC layer temperature (K)

Note that the lower temperature elastic modulus results from Eq. (3.38), which at room temperature are approximately three times less than the Miller et al. (2018) results, appear to be in disagreement with the model basis, Snead et al. (2017), who assume an elastic modulus of 460 GPa for SiC at room temperature. With the source of this apparent discrepancy unknown and the relative agreement of this 460 MPa value to the Ho (1993) data, the Miller et al. (2018) approach of linear interpolation is recommended as

$$E = -5.72678E + 01T + 4.44674E + 05 \tag{3.39}$$

for 293 ≤ T < 1273 K,

$$E = -1.28000E + 02T + 5.30483E + 05 \tag{3.40}$$

for 1273 ≤ T < 1488 K, and

$$E = -3.69091E + 02T + 8.89263E + 05 \qquad (3.41)$$

for 1488 ≤ T < 1873 K.

Snead et al. (2007) note that the dependence of the elastic modulus of SiC irradiation is generally reduced with increasing temperature, and is negligible at temperatures above 1273 K.

Variability is noted for the SiC Poisson's ratio. Ho (1993) recommend a value of 0.13, but also noted a reference value of 0.18. Snead et al. (2007) likewise note a range of Poisson's ratio values for SiC from 0.13 to 0.20, but reference a value of 0.21 as best representing the SiC of TRISO particles. IAEA (2012), Miller et al. (2018), and Hales et al. (2020) assign SiC a Poisson's ratio of 0.13. Given the common application, a Poisson's ratio of 0.13 is suggested for SiC.
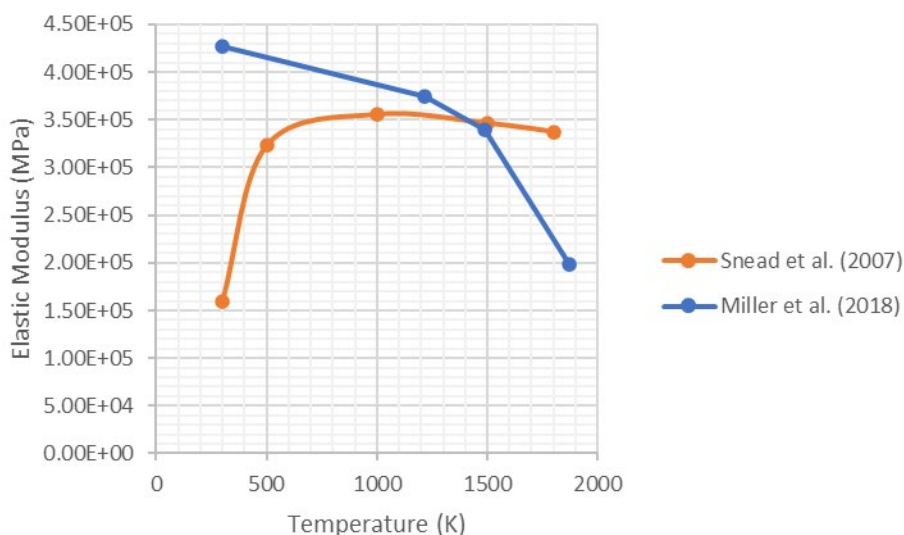
Figure 3.10. Elastic Modulus of SiC as a function of Temperature

3.4.7   Strength and Weibull Modulus

There is substantial variability in the literature for the Weibull parameters of strength and modulus of SiC. Ho (1993) reports a range of 2 to 9.4 for the Weibull modulus at ~ 293 K for various specimen geometries and test methodologies, and recommend a value of m = 6 for temperatures at less than 1250 K. A value of m = 10 was specified at temperatures ≥ 1250 K. A similarly broad range for the Weibull modulus of SiC at m = 3 to 13.8 at ~ 293 K is shown in the data reported in Snead et al. (2007), again attributed to test methods, and they summarize that the Weibull modulus for the TRISO SiC layer is in the range of 4-6 over the "wide temperature range of interest."

IAEA (2012) assigns a value of 6 to the Weibull modulus for irradiated SiC, and a Weibull modulus of 8.02 is specified therein for unirradiated condition. Kovacs et al. (1985) provide a comparative evaluation of the Weibull parameters that describe the SiC fracture strength distribution for failure when the maximum stress exceeds the fracture stress and measured

fracture strength values. They conclude that a Weibull modulus m = 7, with a corresponding median fracture strength of 350 MPa, defines the midrange SiC fracture strength distribution most representative for TRISO SiC.

Ho (1993) reports the room-temperature-strength SiC varies from 60 to over 3100 MPa, and that one contributor to this variation is the stress/volume effect described therein. Over the range of Weibull modulus values defined above from Snead et al. (2007), the "characteristic strength" varies from approximately 500 to 620 MPa, and they have a total characteristic strength range of 205 to 3170 MPa reported (corresponding to m = 1.9 and 8.4, respectively). At the Ho (1993) recommended Weibull modulus of 6, IAEA (2012) has a corresponding mean strength of 572 MPa for the irradiated condition (873 MPa for the m = 8.02 unirradiated condition).

For conservatism, i.e., low strength, and to represent an irradiated condition, a constant value of 350 MPa is recommended for SiC mean failure stress with a corresponding value of 7 for the Weibull modulus.

3.5 Graphite Matrix

Material properties for the graphite matrix are summarized although the matrix is not currently incorporated into Geelhood et al. (2021).

3.5.1 Thermal Conductivity

Miller et al. (2018) describe the thermal conductivity of the graphite matrix, referenced to Gontard and Nabielek (1990), as a function of temperature, irradiation, and packing fraction of TRISO particles within the matrix, and material density, by

$$k = k_T k_\varphi k_{PF} k_\rho \tag{3.42}$$

where:
T = matrix temperature (°C)
φ = fluence (n/m^2, E > 0.18 MeV)/1.52×10^{25} n/m^2
PF = packing fraction (number of particles × particle volume/total compact volume), 0.06 to 0.33 range depending on specific fuel IAEA (2012)
ρ = matrix density (1.7 g/mL, see Section 3.5.2)

$$k_T = k_{100}\left[1 - \alpha(T - 100)e^{\delta T}\right] \tag{3.43}$$

The constant terms in Eq. (3.43) are provided in Hales et al. (2020) as functions of the material type and heat treatment temperature, Table 3.3.

Table 3.3. Matrix Thermal Conductivity Constants (Hales et al. 2020)

Kernel Lot	Heat Treatment Temperature (°C)	k_{100}	α	δ
A3-3	1800	50.8	1.181×10^{-3}	-7.8453×10^{-4}
A3-3	1950	64.6	1.4079×10^{-3}	-9.0739×10^{-4}
A3-27	1800	47.4	9.7556×10^{-4}	-6.0360×10^{-4}
A3-27	1950	62.2	1.4621×10^{-3}	-9.6050×10^{-4}

The functionality with fluence is given by

$$k_\varphi = 1 - \left[0.940 - 0.604 \left(\frac{T}{1{,}000}\right)\right]\left[1 - e^{-\left[2.960 - 1.955\left(\frac{T}{1{,}000}\right)\right]}\right]$$
$$- \left[0.043 \left(\frac{T}{1{,}000}\right) - 0.008 \left(\frac{T}{1{,}000}\right)^2\right]\varphi$$

(3.44)

and the functionality with packing fraction is updated in Hales et al. (2020) to account for broader variability in the packing fraction of the fuel as

$$k_{PF} = \frac{1 + 2\beta PF + (2\beta^3 - 0.1\beta)PF^2 + 0.05PF^3 e^{4.5\beta}}{1 - \beta PF}$$

(3.45)

where

$$\beta = \frac{4.13 - k_T}{4.13 + 2k_T}$$

(3.46)

The functionality with density is expressed with respect to a reference density of 1.7 g/mL as

$$k_\rho = \frac{matrix\ density}{1.7}$$

(3.47)

3.5.2 Density

The reference density for the graphite matrix used in Miller et al. (2018) is 1.7 g/mL, which is consistent with the minimum density specifications provided in IAEA (2012). As-fabricated densities reported in IAEA (2012) range from 1.72 to 1.75 g/mL.

3.5.3 Elastic Modulus and Poisson's Ratio

Hales et al. (2020) set the elastic modulus of the matrix to 10 GPa, which is an average value of the radial and tangential values for the A3-3 and A3-27 matrix materials, and the Poisson's ratio to 0.25, listed by Hales et al. (2020) as a typical value for nuclear-grade graphite.

4.0 TRISO Particle Failure Mechanisms

TRISO particles are designed such that each particle acts as its own pressure vessel, able to contain fission products produced in the fuel kernel. To avoid unwanted release of harmful fission products, it is important to understand the potential failure mechanisms of TRISO particles and their critical parameters. In general, failure mechanisms of TRISO fuels are functions of temperature, burnup, fluence, temperature gradient in the particle, and details of the particle design (IAEA 2010). For context, it is noted that of all the known mechanisms leading to fission product release, failures are dominated by manufacturing defects and are due to rigorous control in the fabrication process, with manufacturing defects typically limited to 1 per 100,000 particles (Petti et al. 2004; Marciulescu and Sowder 2019). Further, TRISO particles have not yet been manufactured on an industrial scale in the US. The AGR program used on the order of 1 million TRISO particles, while a single 100 MWt pebble bed reactor design would require on the order of 1 *billion* particles in the core at any given time.

Table 4.1 lists the failure mechanisms leading to fission product release as recognized by Marciulescu and Sowder (2019), Morris et al. (2004), and IAEA (2010). Descriptions of the failure mechanisms are provided in the subsequent sections. For this literature review, only failure mechanisms that are modeled with the thermal-mechanical model of Geelhood et al. (2021) are reviewed in detail for critical limits regarding their failure mechanism. The mechanisms related to chemical-type failures or manufacturing defects are therefore described but critical limits are not defined. In addition, critical limits for the PyC failure mechanisms from swelling, creep, and shrinkage are not listed because, as described in Geelhood et al. (2021), these mechanisms are not included in the current thermal-mechanical modeling. From Table 4.1, therefore, this literature review will address pressure vessel failure and SiC thermal decomposition with regard to critical limits.

Table 4.1. Failure Mechanisms Morris et al. (2004), Marciulescu and Sowder (2019), and IAEA (2010)

Morris et al. (2004)	Marciulescu and Sowder (2019)	IAEA (2010)
• Pressure vessel failure caused by internal gas pressure • Pyrocarbon layer cracking and/or debonding due to irradiation-induced shrinkage that ultimately leads to the failure of the SiC layer • Fuel kernel migration, which leads to interactions with the coating layers • Fission product/coating layer chemical interactions • Matrix/OPyC interaction • As-manufactured defects during fabrication of fuel particles or during pressing of fuel compacts/spheres • Thermal decomposition of the SiC layer at very high temperatures • Enhanced SiC permeability and /or SiC degradation (high burnup considerations) • Chemical attack (ingress accidents) • Reactivity insertion (accident)	• Pressure vessel failure standard particles • Pressure vessel failure of particles with defective or missing coatings • Irradiation-induced failure of the OPyC coating • Irradiation-induced failure of the IPyC coating and potential SiC cracking • Failure of the SiC coating caused by kernel migration in the presence of temperature gradient • Failure of SiC coating caused by CO/SiC interactions • Failure of the SiC coating resulting from thermal decomposition • Failure of the SiC coating caused by heavy metal dispersion in the buffer and IPyC coating layers	• Overpressure • Irradiation-induced IPyC cracking • Debonding between IPyC and SiC • Kernel migration • Fission product attack • Matrix-OPyC interactions and OPyC irradiation-induced cracking • Non-retentive SiC • Diffusive release trough intact layers • SiC degradation resulting in permeability to fission products • Creep failure of PyC • SiC thermal decomposition • Kernel-coating mechanical interaction

4.1 Pressure Vessel Failure

Pressure vessel failure, refenced to the TRISO particle, not, for example, a reactor vessel, occurs when the tensile stress in the SiC layer exceeds the strength of the SiC layer. Literature sources typically divide pressure vessel failure into Category I and Category II type failures. Category I comprises pressure vessel failures in standard particles that have been made in compliance with their design specifications. Category II comprises defective particles that do not meet design specification. An example of a Category II failure is a particle with an oversized kernel with a thin buffer layer. The literature suggests that particle failure by pressure failure is insignificant and failures that do occur will be dominated by Category II type failures (Verfondern 2012; IAEA 2010).

For Category I failures, the mechanism that leads to pressure vessel failure of the TRISO particle begins during burnup when the kernel generates fission gases. These fission gases are released to the buffer layer, where they are received into the buffer pore space. Proper buffer thickness and porosity are key to mitigating pressure buildup that can lead to pressure vessel failure. The IPyC, SiC, and OPyC layers of the particle work together as structural layers that retain the increasing pressure from the continual generation of fission during irradiation. Irradiation causes the IPyC and OPyC layers to shrink and creep, and the SiC layer exhibits an elastic response. The shrinking IPyC layer pulls the SiC layer toward the kernel opposing the force of the increasing pressure from the fission gases. The shrinking OPyC also helps to oppose the pressure force from the fission gases by pushing the SiC layer inward toward the kernel.

Figure 4.1, from Petti et al. (2004), illustrates this interaction. Particle failure occurs when the stress from the internal pressure exceeds the fracture strength of the SiC layer. The SiC failure results in an instantaneous release causing the simultaneous failure of the IPyC and OPyC layers (Verfondern 2012). Figure 4.2 is an example of a TRISO particle that experienced pressure vessel failure.

IPyC   **SiC**   **OPyC**

shrinks and creeps   elastic   shrinks and creeps

Gas Pressure

1   2   3

1   Gas pressure is transmitted through the IPyC

2   IPyC shrinks, pulling away from the SiC
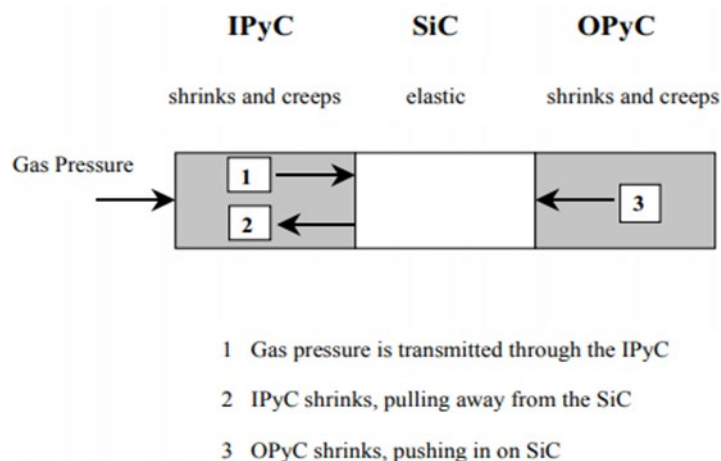
3   OPyC shrinks, pushing in on SiC

Figure 4.1. Pressure Vessel TRISO Layer Interaction (Petti et al. 2004)
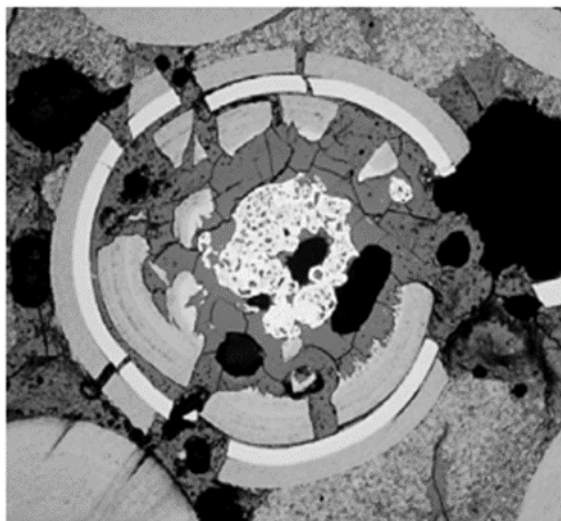
Figure 4.2. Pressure Vessel Failed TRISO Particle Example (Verfondern 2012)

4.1.1 Failure Limits Associated with Reactor Conditions

The reactor conditions associated with pressure vessel failure are temperature, burnup, and fast fluence. Included below are reactor conditions established by the Next Generation Nuclear Plant (NGNP) program as well as operating envelopes used by the programs in Japan and Germany for comparison against parameters explored in this literature review. The limits provided below have been established to prevent and mitigate the release of radiological source terms to the environment.

Table 4.2. Operating Envelope Limits for Reactor Conditions (Marciulescu and Sowder 2019)

Program	Time Averaged Temperature (°C)	Burnup (%FIMA)	Fluence x 10^{25} n/m^2 (E > 0.18 MeV)
NGNP	1250	20	5
Japan	1200	5	3
Germany	1100	15	3

4.1.1.1 Reactor Temperature Effects

Under normal operation temperature, thermal decomposition is not an important contributor to fuel failure. The robustness of UCO fuel as it pertains to temperature can be seen in two tests performed for the AGR Fuel Development and Qualification Program: AGR-1 and AGR-2. UCO fuel performed very well far beyond the NGNP envelope of 1250°C. Table 4.3 lists the combined data from AGR-1 and AGR-2 for 1600°C and 1800°C.

Other failure rates for LEU UCO particle design fuel at high temperatures were found in Kovacs et al. (1983). Kovacs et al. (1983) reported failure rates at 1600°C for Category I and Category II pressure vessel failure modes of 0.6 x 10^{-3} and 2.6 x 10^{-3}, respectively.

Table 4.3. SiC Layer Failures as a Function of Temperature (Marciulescu and Sowder 2019)

Test Condition	Number of Compacts	Number of Particles	Number of Failures	Failure Fraction	95% Confidence
			SiC Layer Failures		
Irradiation	108	412,336	8	1.9×10^{-5}	$\leq 3.6 \times 10^{-5}$
1600°C	12	45,804	3	6.5×10^{-5}	$\leq 1.7 \times 10^{-4}$
1800°C	7	26,028	24	9.2×10^{-4}	$\leq 1.3 \times 10^{-3}$

4.1.1.2   Reactor Burnup Effects

Fuel burnup determines the quantity of fission products in the kernel, which affects both the gas pressure and the fission product concentration in the particles that can interact with the coating layers. Kovacs et al. (1983) documented pressure vessel failures for candidate fissile fuels tested in Capsule HRB-16, found fuel types exhibited random failure fluctuation, and observed no systematic pressure vessel failure as a function of burnup for any fuel. Failure rates for various burnup rates and the various UCO fuel types are listed in Table 4.4.

Table 4.4. Summary of UCO Data. Adapted from Kovacs et al. (1983)

TRISO Coated Kernel	Fuel Description	Temp (°C)	Burnup (%FIMA)	Fluence $[10^{23}$ n/m^2(E > 29 fJ) $_{HTGR}]$	Visually Determined Particle Failure Fraction	Category I Predicted Pressure Vessel Failure Fraction
		Irradiation Conditions				
$UC_{0.5}O_{1.5}$	Parent batch material	1283	27.6	6.3	0.010	5×10^{-5}
$UC_{0.5}O_{1.5}$	No OPyC most faceted	1284	27.4	6.2	0.010	7×10^{-4}
$UC_{0.5}O_{1.5}$	No OPyC nonfaceted	1284	27.4	6.2	0.036	7×10^{-4}
$UC_{0.5}O_{1.5}$	No OPyC most faceted	1274	24.1	5.0	0.019	1×10^{-4}
$UC_{0.5}O_{1.5}$	No OPyC nonfaceted	1274	24.1	5.0	0.010	1×10^{-4}

UCO data from AGR-1 and AGR-2 fuel performance tests was also reviewed. Average burnup was below the NGNP envelope as listed in Table 4.5. AGR-1 had no failures in 300,000 particles and AGR-2 had four failures of 114,000 particles (Marciulescu and Sowder 2019).

Table 4.5. Average Burnup (%FIMA) for AGR-1 and AGR-2 Fuel (adapted from Marciulescu and Sowder 2019).

Capsule	Capsule Average Burnup (%FIMA)
AGR1 – UCO Fuel	
1	15.3
2	17.8
3	18.6
4	18.2
5	16.5
6	13.4
AGR2 – UCO Fuel	
2	12.2
5	11.7
6	9.3

Hales et al. (2020) provide data for the extended burnup of LEU UCO fuel, and the BISON code was used to model Coordinated Research Project (CRP) – 6 Case 12. The input parameters for the model can be found in Stawicki (2006). Hales et al. (2020) compared the results from BISON code with the outputs for STRESS3, ATLAS, and PARFUME showing tangential SiC stress as a function of burnup. Over a range of 0-80% FIMA, all codes showed stresses below 0 MPa with exception of the STRESS3 code.

4.1.1.3 Reactor Fast Fluence Effects

Reactor fast fluence impacts the level of radiation damage in the particles and the potential changes in properties and dimensions in the layers (Marciulescu and Sowder 2019). Based on findings in Ketterer and Bullock (1981) and discussed in IAEA (2010), spherical fuel elements exposed to higher fluence (4×10^{25} -6×10^{25} n/m^2) and higher burnup (14% FIMA) have exhibited a greater release of fission products (e.g., cesium) in heating tests compared with similar spheres exposed to conditions inside the German program operating envelope (8-9% FIMA, 2-4 x 1025 n/m^2). Figure 4.3 illustrates the increase in failure of coatings as a function of fluence.
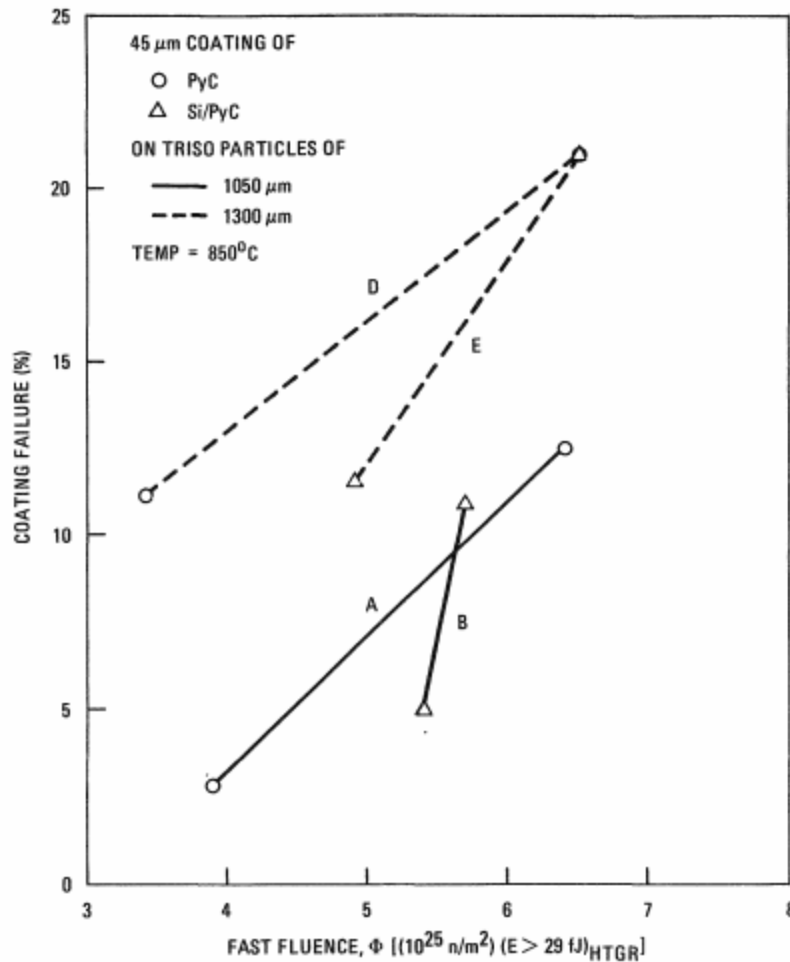
Figure 4.3. Outer Coating Failure as a Function of Fluence for Two Sizes of Particles with Two Different Type of Coatings (Ketterer and Bullock 1981)

4.1.2   Particle Design Parameters Affecting Pressure Vessel Failure

According to IAEA (2010), the particle design parameters that influence pressure vessel failure are the strength of the SiC layer, fission gas release, and buffer density and layer thickness. The literature is reviewed for the particle design parameters, noting critical limits where possible.

4.1.2.1   Strength of SiC layer

Weibull theory is widely used to predict particle layer failures (e.g., Petti et al. 2004; IAEA 2010; Miller et al. 2018). Weibull parameters for the SiC layer are provided in Section 3.4.7.

4.1.2.2   Fission Gas Release

Fission gases released during irradiation from the kernel of a coated particle depend on temperature, burnup, and time (Petti et al. 2004). Gas pressure from fission gases generated in the kernel is transmitted through the IPyC layer to the SiC. This pressure continually increases as irradiation of the particle progresses, thereby contributing to a tensile hoop stress in the SiC layer. Fission gas pressure increases with an increase in temperature and/or burnup. To

illustrate the trend of temperature and burnup, Table 4.6 provides the data from Petti and Maki (2005), which displays the normalized fission gas that builds in a 500-μm German UO_2 particle as a function of temperature and burnup. Over the conditions tested, the relative pressure increase from burnup exceeds that of temperature.

Table 4.6. Normalized Fission Gas Pressure in a German Program Particle as Temperature and Burnup Are Increased (normalized to 1.0 at 8% FIMA and 1100°C) (from Petti and Maki 2005)

	Temperature (°C)				
Burnup	1100	1150	1200	1250	1300
8%	1.00	1.28	1.62	2.04	2.52
10%	1.33	1.69	2.14	2.68	3.28
15%	2.26	2.86	3.60	4.47	5.42
20%	3.32	4.21	5.28	6.53	7.89

The major contributor to internal pressure, specifically in UO_2 fuel kernels, is CO. CO can dominate the percentage of the internal pressure by as much as four times more than the contribution from the other gases (Petti and Maki 2005). CO is formed when the oxygen released during fission reacts with the carbonaceous buffer layer to form CO gas. Pressure as a result of fission gases is significantly different in UCO fuel. The UCO fuel particle controls the CO pressure by using carbide within the kernel, which can be preferentially oxidized (Zhou and Tang 2011). A comparison of gas pressure from the German program UO^2 and UCO fuel is illustrated below. The UCO particle operates at a much lower pressure and contributes far less to the total gas pressure from CO.

(a)   (b)
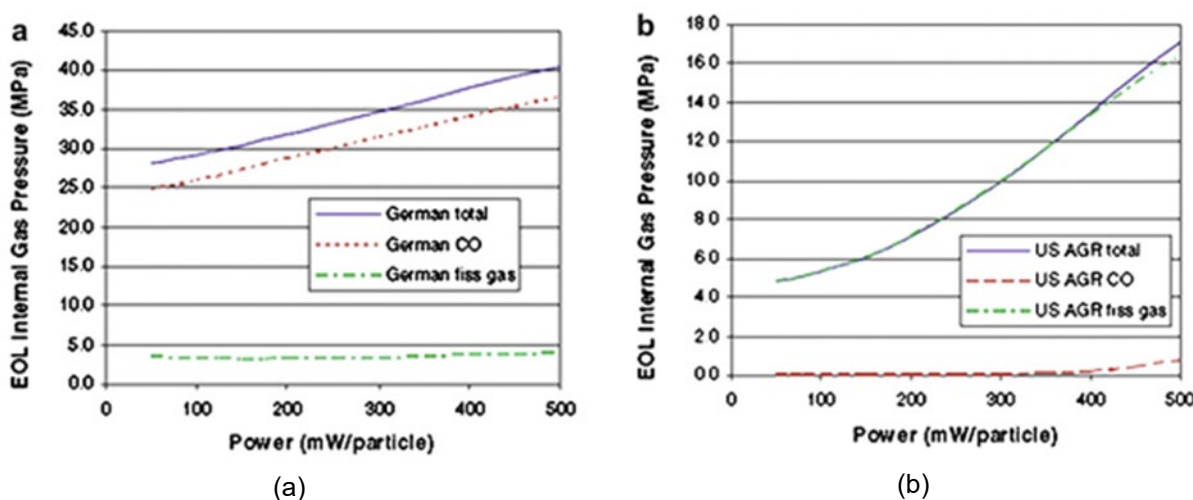
Figure 4.4. (a) Fission Gas Pressure in a German Program UO^2 Kernel TRISO Particle; (b) Fission Gas Pressure in a U.S. Program UCO Kernel TRISO Particle (Petti and Maki 2005)

With respect to the CO production from UCO fuel, IAEA (2010) notes that "UCO fuel eliminates CO" production, and Marciulescu and Sowder (2019) reference UCO as the fissile kernel of choice because of its ability to limit CO production. Further, note data that indicate the efficacy

of UCO fuel in limiting the oxygen partial pressure and the subsequent formation of carbon monoxide.

McMurray et al. (2017) developed general oxygen balance formulas for calculating the minimum UCx content to ensure negligible CO formation to preclude the failure mechanisms resulting from high O_2 and CO pressures. When applied to UCO HTGR fuel-enriched to 15.5% FIMA and taken to 16.1% FIMA, 5.1–5.5 mole% UCx is indicated as the minimum initial content needed to maintain acceptably low CO pressure. For reference, the composition of UCO kernels as reported in IAEA (1020) has a range of composition 65-85 mol% UO_2 and 15-35 mol% UCx. The AGR fuel used UCO kernels with a composition of 68-71 mol% UO_2 and 28-32 mol% UCx and limited internal pressure build up (Dewi et al 2020). Skerjanc (2019) notes that CO contributes negligibly to the internal pressure in TRISO fuel particles for a starting kernel composition ($UO_2/UC_2=3$).

The Proksch and Strigle (1982) O_2 release model for UO_2 fuel is widely applied throughout the TRISO literature, and is given by

$$log\left[\left(\frac{O}{f}\right)t^2\right] = -0.21 - \frac{8500}{T + 273} \qquad (4.1)$$

where:
O/f = oxygen release at the end of irradiation (atoms per fission)
t = irradiation time (days)
T = time-averaged particle surface temperature during irradiation (°C)

Miller et al. (2018) provide expressions for the CO production from both UO_2 and UCO fuel as functions of the kernel temperature, burnup, U-235 enrichment, and carbon-to-uranium ratio. These expressions are derived from thermochemical free energy minimization calculations performed by the HSC code (see Skerjanc 2019).

4.1.2.3   Buffer Density

The low-density porous buffer is responsible for absorbing fission recoils, containing fission gases, and accommodating kernel swelling. The buffer layer must have sufficient thickness and low density to provide adequate void space in order to manage pressure within the particle. No literature was found specifying critical limits for the porosity of the buffer. A discussion of the buffer layer density values is provided in Section 3.2.4.

4.1.2.4   Buffer Layer Thickness

Marciulescu and Sowder (2019) state that buffer thickness is the critical parameter for TRISO fuels based on findings from Skerjank et al. (2016). Critical manufacturing limits were identified by Skerjank et al. (2016) using PARFUME with regard to LEU TRISO nuclear fuel UCO particles with a kernel diameter of 425 µm. The key findings for layer thickness are as follows:

- *SiC thickness*: When varying the thickness of the SiC layer, the failure probability increased as the thickness decreased. This can be attributed to less structural material to retain the fission gas pressure and subsequent increase in tangential stress in the layer.

- *IPyC thickness*: Conversely, failure probability increased as the IPyC layer thickness increased. This is due to the increase in pyrocarbon material causing an increase in shrinkage early in irradiation. This results in a higher IPyC cracking probability causing localized stress concentrations in the SiC layer.

- *Buffer thickness*: As the buffer thickness increases, the volume available to store fission gas increases, resulting in a lower pressure and hence less stress in the SiC layer.

Table 4.7 compares the critical values for thickness from Skerjank et al. (2016) to the design parameters for U.S. fissile and fertile fuels from IAEA (1997). The listed temperature values are the irradiation temperature that produced a higher failure probability which resulted in the reported critical limit. The design parameters are shown to protect the particles from failure relative to the listed critical layer thickness limits.

Table 4.7. Critical Layer Thickness from Skerjank et al. (2016) Compared to Design Parameters from (IAEA 1997)

Layer	Range of Values Analyzed (μm)	Temperature Value (K)	Critical Limit (μm)	U.S. UCO Fissile 20% Enriched Design Dimensions (μm)	U.S. UCO Fertile Fuel Design Dimensions (μm)
IPyC thickness	10-70	1173	52	35	35
SiC thickness	10-60	1173	20	35	40
Buffer thickness	10-150	1523	50	100	65

4.1.3   Pressure Vessel Failure Summary

Table 4.8 lists the reactor conditions and the particle design parameters that affect pressure vessel failure, along with model codes that include pressure vessel failure. Summary discussion of the failure limits for the reactor and particle conditions is provided.

Table 4.8. Pressure Vessel Failure Summary (IAEA 2010) and Model Summary (Powers and Wirth 2010)

Failure Mechanism	Reactor Conditions Contributing to Failure Mechanism	Particle Design Parameters Contributing to Failure Mechanism	Models with Mechanism
• Pressure vessel failure	• Temperature • Fast fluence • Burnup	• Strength of SiC • Buffer density (void volume) • Fission gas release, CO production, and kernel type • Layer thickness	• PARFUME • PASTA • ATLAS • STRESS3 • TIMCOAT • GA/KFA • JAERI • BISON

4.1.3.1   Reactor Conditions

- *Temperature*: The NGNP design envelope is 1250°C. AGR-1 and AGR-2 test runs performed well with UCO fuel at temperatures up to 1800°C.

- *Burnup*: The NGNP design envelope for UCO is 20% FIMA.

- *Fast fluence*: The NGNP design envelope for UCO is 5 x 10^{25} n/m^2.

Particle Design Parameters

- *Strength of SiC*: No limits are identified.

- *Buffer density/void volume*: The critical parameter for void volume is approached by using buffer thickness as most sources assume a buffer density of 50%.

- *Fission gas*: A majority of the internal pressure comes from CO generation, which is mitigated by having carbide in the kernel to mitigate oxygen migrating to the buffer layer where it becomes CO.

- *Layer thickness*: From Skerjank et al. (2016), SiC has a critical minimum thickness of 20 μm, the buffer layer has a minimum critical thickness of 50 μm, and IPyC has a maximum critical thickness of 52 μm.

4.2   SiC Thermal Decomposition Failure

The phenomenon of SiC thermal decomposition failure is primarily a function of temperature and time and has not played a major role in fuel failure at lower accident temperatures of 1600°C, where safety testing has been routinely performed (Morris et al. 2004). Fuel releases generally increase at temperatures above 1600°C, with releases at 1800°C being much greater (Morris et al. 2004).

Temperature data for SiC thermal decomposition at elevated temperatures from (Zhou and Tang 2011) was reviewed. Zhou and Tang (2011) concluded that temperatures that are kept higher than 1600°C for extended duration can lead to high fuel failure rates, and that above 2000°C SiC coatings decompose rapidly. Zhou and Tang (2011) summarize fuel tests performed by others on irradiated coated fuel particles tested to 2600°C. Results are shown in Figure 4.5; failures started above approximately 1800°C and all particles were failed at 2600°C.

Table 4.9 lists the reactor conditions and the particle design parameters that affect SiC thermal decomposition failure, along with model codes that include SiC thermal decomposition.
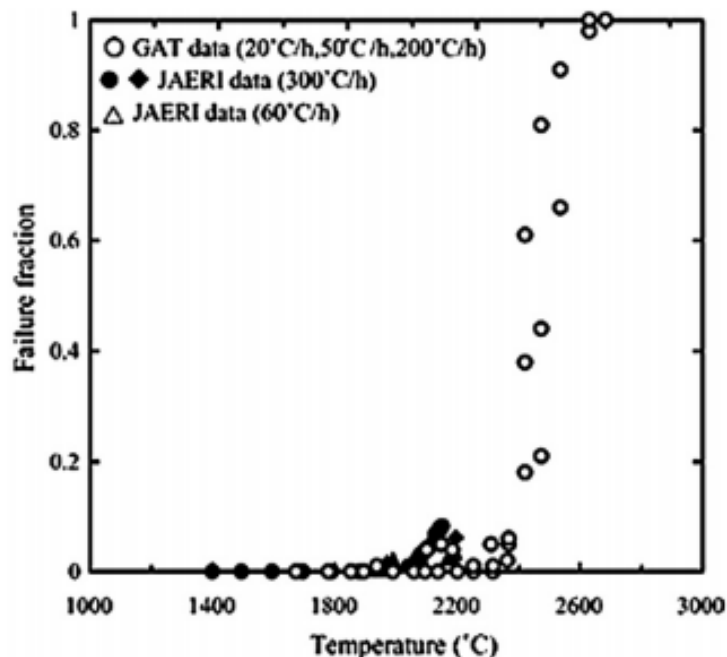
Figure 4.5. Failure Fraction as a Function of Temperature for Coated Fuel Particles (Zhou and Tang 2011)

Table 4.9. SiC Thermal Decomposition Failure Summary (IAEA 2010) and Model Summary (Powers and Wirth 2010)

Failure Mechanism	Reactor Conditions Contributing to Failure Mechanism	Particle Design Parameters Contributing to Failure Mechanism	Models with Mechanism
• SiC thermal decomposition	• Temperature • Time at temperature	• SiC Thickness • Microstructures of SiC	• PARFUME

4.3   Irradiation Induced IPyC Cracking Failure

The factors influencing the irradiation induced cracking failure of the IPyC are shrinkage, swelling, and creep, and the IPyC cracking has been attributed to high anisotropy of the PyC layer (Morris et al. 2004). Cracking of the IPyC layer may occur during irradiation induced shrinkage due to the resultant buildup of internal stresses. Cracks in the IPyC layer develop when the internal stresses become greater than the fracture strength.

Table 4.10 lists the reactor conditions and the particle design parameters that affect irradiation-induced IPyC cracking failure, along with the model codes that include irradiation-induced IPyC cracking.

Table 4.10. Irradiation-Induced IPyC Cracking Failure Summary (IAEA 2010) and Model Summary (Powers and Wirth 2010)

Failure Mechanism	Reactor Conditions Contributing to Failure Mechanism	Particle Design Parameters Contributing to Failure Mechanism	Models with Mechanism
• Irradiation-induced IPyC cracking	• Temperature • Fast fluence	• Dimensional change of PyC • Irradiation induced creep of PyC • Anisotropy	• PARFUME • PASTA • ATLAS • STRESS3 • TIMCOAT • GA/KFA • JAERI • BISON

4.4 Debonding between IPyC and SiC Layers Failure

Debonding of the IPyC and SiC interface is related to the nature of the IPyC/SiC interface (Morris et al. 2004). Debonding occurs when the radial stress that develops between the IPyC and SiC layers, due to shrinkage of the IPyC layer, exceeds the bond strength between layers (Miller et al, 2004). (Miller et al, 2004) concluded that the debonding process is likely a progressive unzipping of the two layers that starts at a week point on the interface between the layers. Debonding of the IPyC and SiC can lead to larger tensile stresses in the SiC, which in turn can lead to SiC failure. SiC failure rates are low, but not insignificant, for debonding of the IPyC and SiC (Morris et al. 2004).

Table 4.11 lists the reactor conditions and the particle design parameters that affect debonding of the IPyC and SiC interface failure, along with model codes that include debonding of the IPyC/SiC interface.

Table 4.11. Debonding Between IPyC and SiC Layers Failure Summary (IAEA 2010) and Model Summary (Powers and Wirth 2010)

Failure Mechanism	Reactor Conditions Contributing to Failure Mechanism	Particle Design Parameters Contributing to Failure Mechanism	Models with Mechanism
• Debonding between IPyC and SiC layers	• Temperature • Fast fluence	• Nature of the interface • Interfacial strength • Dimensional change of PyC • Irradiation-induced creep of PyC	• PARFUME • ATLAS • STRESS3

4.5 Kernel Migration Failure

Kernel migration is the movement of the kernel in the coated particle toward the TRISO coating. A kernel that penetrates the TRISO coating will lead to the failure of the particle. Kernel migration occurs when a thermal gradient exists across the particle and the chemical equilibrium C/CO is different on each side of the particle. Mass transport of CO is moved down the temperature gradient and the kernel is moved up the temperature gradient. Kernel migration is primarily dependent on the temperature and the macroscopic temperature gradient in the fuel,

with a secondary dependance on burnup (Morris et al. 2004). Power densities in prismatic cores with UO_2 fuel have an increased potential for the kernel to migrate (Morris et al. 2004). Because thermal gradients are smaller in pebble bed reactors, kernel migration is less likely. Kernel migration has been mitigated by using UCO-type fuel kernels that eliminate problems from CO production.

Table 4.12 lists the reactor conditions and the particle design parameters that affect kernel migration, along with model codes that include kernel migration.

Table 4.12. Kernel Migration Failure Summary (IAEA 2010) and Model Summary (Powers and Wirth 2010)

Failure Mechanism	Reactor Conditions Contributing to Failure Mechanism	Particle Design Parameters Contributing to Failure Mechanism	Models with Mechanism
• Kernel migration	• Temperature • Burnup • Temperature gradient	• Layer thickness • Kernel type	• PARFUME

4.6 Fission Product Attack Failure

Fission products, specifically palladium and silver, can migrate from the kernel and interact with the SiC layer, potentially causing damage. This phenomenon is not well understood, but it is known that fission product attack is a function of temperature, temperature gradient, and burnup reactor conditions. The degree of fission attack is generally correlated to temperature and temperature gradient of the fuel (Morris et al. 2004). It tends to be more significant for UO_2 fuel as UCO fuels tend to limit the mobility of fission products (Morris et al. 2004).

Table 4.13 lists the reactor conditions and the particle design parameters that affect fission product attack failure, along with model codes that include fission product attack.

Table 4.13. Fission Product Attack Failure Summary (IAEA 2010) and Model Summary (Powers and Wirth 2010)

Failure Mechanism	Reactor Conditions Contributing to Failure Mechanism	Particle Design Parameters Contributing to Failure Mechanism	Models with Mechanism
• Fission product attack	• Temperature • Burnup • Temperature gradient • Time at temperature	• Fission product transport behavior • Diffusion • Buffer densification and cracking • Chemical state/transport behavior of fission products • Microstructure of PyC and SiC	• None indicated

4.7 Non-retentive SiC Failure

Morris et al. (2004) describe non-retentive SiC failure as not a formally considered structural failure mechanism. There is limited evidence that fluence and/or burnup play a role in the permeability or degradation of the SiC layer with respect to fission products during high-temperature heating (Morris et al. 2004). IAEA (2010) breaks this mechanism down into two different cases: (1) diffusive release through intact SiC, and (2) degradation of the SiC layer, resulting in measurable SiC permeability. The two mechanisms of degradation of the SiC layer reported in IAEA (2010) are corrosion by CO and degradation by cesium. Corrosion by CO is assumed to happen at elevated temperatures if the IPyC layer is porous or cracked, and degradation by cesium has limited data and the exact mechanism is not clear. Morris et al. (2004) suggest that as particles are pushed to higher burnup, this phenomena may become a larger issue.

Table 4.14 lists the reactor conditions and the particle design parameters that affect non-retentive SiC failure, along with model codes that include non-retentive SiC.

Table 4.14. Non-retentive SiC Layer Failure Summary (IAEA 2010) and Model Summary (Powers and Wirth 2010)

Failure Mechanism	Reactor Conditions Contributing to Failure Mechanism	Particle Design Parameters Contributing to Failure Mechanism	Models with Mechanism
• Non-retentive SiC: diffusion through intact layers	• Burnup • Fast fluence • Temperature • Temperature gradient • Time at temperature	• Chemical state/transport behavior of fission products • Microstructure of SiC • SiC thickness	• None indicated
• Non-retentive SiC: degradation of SiC	• Burnup • Temperature • Fluence • Time at temperature	• Kernel type (UCO, UO$_2$) • IPyC performance • Microstructure of SiC • Thickness of SiC	• None indicated

4.8 Creep Failure of PyC

Some post irradiation heating tests revealed thinned and failed PyC (IAEA 2010). These results were determined for tests with temperatures greater than 2000°C for long durations, and the observed failures did not lead to failure of the SiC layer.

Table 4.15 lists the reactor conditions and the particle design parameters that affect creep failure of PyC, along with model codes that include creep failure of PyC.

Table 4.15. PyC Thermal Creep Failure Summary (IAEA 2010) and Model Summary (Powers and Wirth, 2010)

Failure Mechanism	Reactor Conditions Contributing to Failure Mechanism	Particle Design Parameters Contributing to Failure Mechanism	Models with Mechanism
• PyC thermal creep	• Time at temperature	• Thickness of PyC and stress state of PyC	• None indicated

4.9 Kernel-Coating Mechanical Interaction Failure

At high burnup values, gaps between the kernel and coatings close when the kernel swells, resulting in a mechanical interaction between the layers. This is termed a kernel-coating mechanical interaction (KCMI). This failure has not been reported experimentally (IAEA 2010). IAEA (2010) states that modeling efforts have predicted that the SiC layer will fail quickly after the onset of KCMI, but no modeling efforts were indicated by Powers and Wirth (2010) . IAEA (2010) notes that this failure mechanism may be a bigger factor as the limits of higher burnup values are attempted.

Table 4.16 lists the reactor conditions and the particle design parameters that affect KCMI, along with model codes that include KCMI.

Table 4.16. Kernel Coating Mechanical Interaction Failure Summary (IAEA 2010) and Model Summary (Powers and Wirth 2010)

Failure Mechanism	Reactor Conditions Contributing to Failure Mechanism	Particle Design Parameters Contributing to Failure Mechanism	Models with Mechanism
• Kernel coating mechanical interaction	• Burnup • Fast fluence • Temperature	• Initial kernel – coating gas gap • Buffer properties • IPyC properties • Kernel swelling rate	• None indicated

5.0 References

Bates JL. 1969. *Thermal Conductivity and Electrical Resistivity of Uranium Oxycarbide*. BNWL-989. Battelle Memorial Institute, Pacific Northwest Laboratory, Richland, Washington.

Chiotti P, WC Robinson, and M Kanno. 1966. "Thermodynamic Properties of Uranium Oxycarbides." *Journal of Less-Common Metals* 10(1966):273-289

DeConinck R, W Van Lierde, and A Gus. 1975. "Uranium Carbide: Thermal Diffusivity, Thermal Conductivity, and Spectral Emissivity at High Temperatures." *Journal of Nuclear Materials* 57(1975):69-76.

Dewi AK, S Yamaguchi, T Onitzuka, and M Uno. 2020. *"Thermal conductivity calculation of ZrCeZrO$_2$ pellet from powder metallurgy as the surrogate of UCO kernel fuel." Journal of Nuclear Materials* 539(2020):152343.

Devida C, M Betti. P Peerani, EH Toscano, and W Goll. 2004. *Quantitative Burnup Determination: A Comparison of Different Experimental Methods*. "HOTLAB" Plenary Meeting 2004, September 6th - 8th, Halden, Norway.

Ebner MA. 2004. *Chemistry Improvement for the Production of LEU UCO Fuel Using Manufacturing Scale Equipment – FY2004 Final Report*. INEEL/EXT-04-02372. Idaho National Engineering and Environmental Laboratory, Bechtel BWXT Idaho, LLC, Idaho Falls, Idaho.

Geelhood KJ, WG Luscher, IE Porter, L Kyriazidis, CE Goodson, and EE Torres. 2020. *MatLib-1.0: Nuclear Material Properties Library*. PNNL-29728. Pacific Northwest National Laboratory, Richland, Washington.

Geelhood KJ, BE Wells, and NR Phillips. 2021. *FAST-TRISO Code Description Document*. PNNL-31426. Pacific Northwest National Laboratory, Richland, Washington.

Gontard R and H Nabielek. 1990. *Performance Evaluation of Modern HTR TRISO Fuels*. HTA-IB-05/90, Julich, July 31, 1990.

Hales JD, W Juang, A Toptan, and K Gamble. 2020. *BISON TRISO Modeling Advancements and Validation to AGR-1 Data*. Report INL/EXT-20-59368. Idaho National Laboratory, Idaho Falls, Idaho.

Haynes WM, ed. 2011. *CRC Handbook of Chemistry and Physics* (92nd ed.). Boca Raton, Florida: CRC Press. p. 4.88. ISBN 1439855110.

Ho F. 1993. *Material Models or Pyrocarbon and Pyroloytic Silicon Carbide*. CEGA-002820, Rev. 1. WBS: 2.9.7.1. CEGA Corporation, San Diego, California.

Hollenberg GW, CH Henager Jr., GE Youngblood, DJ Trimble, SA Simonson, GA Newsome, and E Lewis. 1993. *The Effect of Irradiation on the Stability and Properties of Monolithic Silicon Carbide and SiCf/SiC Composites up to 25 dpa*. PNL-SA-23607. Pacific Northwest Laboratory, Richland, Washington.

IAEA. 1997. *Fuel Performance and Fission Product Behaviour in Gas Cooled Reactors*. IAEA-TECDOC-978. International Atomic Energy Agency, Vienna, Austria.

IAEA. 2010. *High Temperature Gas Cooled Reactor Fuels and Materials*. IAEA-TECDOC-1645. International Atomic Energy Agency, Vienna, Austria.

IAEA. 2012. *Advances in High Temperature Gas Cooled Reactor Fuel Technology*. IAEA-TECDOC-1674. International Atomic Energy Agency, Vienna, Austria.

Jolly B, T Lindemer, and K Terrani. 2015. *M3FT-15OR0202237: Submit Report on Results from Initial Coating Lyer Development for UN TRISO Particles*. ORNL/LTR-2015/87. Oak Ridge National Laboratory, Oak Ridge, Tennessee.

Ketterer JW and RE Bullock. 1981. *Capsule HRB-15B Postirradiation Examination Report*. GA-A15940. GA Technologies.

Kovacs WJ, K Bongartz, and DT Goodin. 1983. *TRISO-Coated HTGR Fuel Pressure Vessel Performance Models*. GA-A16807, UC-77. GA Technologies.

Kovacs WJ, K Bongartz, and DT Goodin. 1985. "High-Temperature Gas-Cooled Reactor Fuel Pressure Vessel Performance Models." *Nuclear Technology* 68(3):344-354. doi:10.13182/NT85-A33580

Lewis HD and JF Kerrisk. 1976. *Electrical and Thermal Transport Properties of Uranium and Plutonium Carbides A Review of the Literature*. UC-25 and UC-79b. Los Alamos Scientific Laboratory, Los Alamos, New Mexico.

Li R, B Liu, and K Verfondern. 2019. The Study of Irradiation-Induced Failure Behavior for the TRISO-Coated Fuel Particle in HTGR. *Journal of Nuclear Materials*. 516 (2019) 214-227.

Liu D, S Knol, J Ell, H Barnard, M Davies, J Vreeling, and RO Ritchie. 2020. "X-ray Tomography Study on the Crushing Strength and Irradiation Behaviour of Dedicated Tristructural Isotropic Nuclear Fuel Particles at 1000 °C." *Journal Materials and Design* 187.

López-Honorato E, C Chiritescu, P Xiao, DG Cahill, G Marsh, and TJ Abram. 2008. "Thermal Conductivity Mapping of Pyrolytic Carbon and Silicon Carbide Coatings on Simulated Fuel Particles by Time-Domain Thermoreflectance." *Journal of Nuclear Materials* 378(2008):35-39.

Ma BM. 1983. *Nuclear Reactor Materials and Applications*. Van Nostrand Reihold Co, New York.

Marciulescu C and A Sowder. 2019. *Uranium Oxycarbide (UCO) Tristructural Isotropic (TRISO) Coated Particle Fuel Performance*. Topical Report EPRI-AR-1 (NP). 3002015750. Electric Power Research Institute, Palo Alto, California.

Maxwell JC. 1873. *A Treatise on Electricity and Magnetism*. Clarendon Press.

McMurray JW, TB Lindemer, NR Brown, TJ Reif, RN Morris, and JD Hunn. 2017. "Determining the Minimum Required Uranium Carbide Content for HTGR UCO Fuel Kernels." *Annals of Nuclear Energy* 104(2017):237-242.

Men'shikova TS, FG Reshetnikov, VS Mukhin, GA Rymashevskii, IG Lebedev, and AL Epshtein. 1971. *Properties of Carbide, Nitride, Phosphide, and other Fuel Compositions and Their Behavior Under Irradiation*. State Committee for the Use of Atomic Energy of the USSR. Translated from *Atomnaya Energiya* 31(4):393-402.

Miller GK, DA Petti, JT Maki, and DL Knudson. 2004. Consideration of The Effects of Partial Debonding of The IPyC and Particle Ashpericity On TRISO-coated Fuel Behavior. *Journal of Nuclear Materials.* 334 (2004) 79-89.

Miller GK, DA Petti, JT Maki, DL Knudson, and WF Skerjanc. 2018. *PARFUME Theory and Model Basis Report*. INL/EXT-08-14497, Rev.1. Idaho National Laboratory, Idaho Falls, Idaho.

Morris RN, DA Petti, DA Powers, and BE Boyack. 2004. *TRISO-Coated Particle Fuel Phenomenon Identification and Ranking Tables (PIRTs) for Fission Product Transport Due to Manufacturing, Operations, and Accidents*. NUREG-6844 Main Report, Vol. 1. U.S. Nuclear Regulatory Commission Regulation, Washington, D.C.

Nagley SG, CM Barnes, DWL Husser, ML Nowlin, and WC Richardson. 2010. *Fabrication of Uranium Oxycarbide Kernels for HTR Fuel*. INL/CON-10-18858. Idaho National Laboratory, Idaho Falls, Idaho.

Olander DR. 1976. *Fundamental Aspects of Nuclear Reactor Fuel Elements*. Technical Information Center, Office of Public Affairs, Energy Research and Development Administration. ISBN 0-87079-031-5 (v.1).

Ortensi J and AM Ougouag. 2009. *Improved Prediction of the Temperature Feedback in TRISO-Fueled Reactors*. INL/ EXT-09-16494. Idaho National Laboratory, Idaho Falls, Idaho.

Petti D and J Maki. 2005. *The Challenges Associated with High Burnup and High Temperature for UO^2 TRISO-Coated Particle Fuel*. MIT NGNP Symposium, February 2005.

Petti D, P Martin, M Phélip, and R Ballinger. 2004. *Development of Improved Models and Designs for Coated-particle Gas Reactor Fuels*. INEEL/EXT-05-02615. Idaho National Engineering and Environmental Laboratory, Idaho Falls, Idaho.

Petti DA, PA Demkowwicz, JT Maki, and RR Hobbins. 2012. *TRISO-Coated Particle Fuel Performance*. INL/JOU-09-16642. Idaho National Laboratory, Idaho Falls, Idaho. United States: N. p., 2012. Web. doi:10.1016/B978-0-08-056033-5.00055-0.

Powers JJ and BD Wirth. 2010. "A Review of TRISO Fuel Performance Models." *Journal of Nuclear Materials* 405(2010):74-82.

Powers JJ. 2011. *TRISO Fuel Performance: Modeling, Integration into Mainstream Design Studies, and Application to a Thorium-fueled Fusion-Fission Hybrid Blanket*. Dissertation for Doctor of Philosophy in Engineering - Nuclear Engineering, University of California, Berkeley, California.

Proksch A and A Strigle. 1982. "Production of Carbon Monoxide During Burn-up of UO_2 Kerneled HTR Fuel Particles." *Journal of Nuclear Materials* 107(1982):280-285.

Richards HK. 1971. "Thermal Expansion of Uranium and Tantalum Monocarbides up to 2700°C." *Nuclear Technology* 10(1):54-61. doi:10.13182/NT71-A30947

Savvatimskiy AI. 2003. Measurements of the Melting Point of Graphite and the Properties of Liquid Carbon (a review for 1963- 2003). *Carbon*. 43 (2005) 1115- 1142.

Senor DJ, DJ Trimble, and JJ Woods. 1996. *Effect of Irradiation on Thermal Expansion of SiCF/SiC Composites*. KAPL-P-000055 (K96074). KAPL Atomic Power Laboratory, Schenectady, New York.

Skerjank WF, JT Maki, BP Collin, and D Petti. 2016. "Evaluation of Design Parameters for TRISO-coated Fuel Particles to Establish Manufacturing Critical Limits Using PARFUME." *Journal of Nuclear Materials*, February 2016.

Skerjank WF. 2019. *CO Production Model Analysis for Correlations into PARFUME*. INL/MIS-19-55748-Revision-0. Idaho National Laboratory, Idaho Falls, Idaho.

Snead LL, T Nozawa, Y Katoh, T-S Byun, S Kondo, and DA Petti. 2007. "Handbook of SiC Properties for Fuel Performance Modeling." *Journal of Nuclear Materials* 371(2007):329-377.

Stawicki M. 2006. *Benchmarking of the MIT High Temperature Gas-Cooled Reactor TRISO-Coated Particle Fuel Performance Mode*. Massachusetts Institute of Technology, Cambridge, Massachusetts.

Tang C, X Fu, J Zhu, H Zhao, and Y Tang. 2012. "Comparison of Two Irradiation Testing Results of HTR-10 Fuel Spheres." *Nuclear Engineering and Design* 251(2012):453-458.

Verfondern K. 2012. *TRISO Fuel Performance Modeling and Simulation*. Institute for Energy Research – Safety Research and Reactor Technology (IEF-6), Julich, Germany.

Wang Y, DH Hurley, EP Luther, MF Beaux II, DR Vodnik, RJ Peterson, BL Bennett, IO Usov, P Yuan, X Wang, and M Khafizov. 2018. "Characterization of Ultralow Thermal Conductivity in Anisotropic Pyrolytic Carbon Coating for Thermal Management Applications." *Carbon* 129(2018):476-485.

Wei H, J Zhang, and S Ding. 2019. "A Model for Effective Thermal Conductivity of Porous Carbon Materials in FCM Fuel Pellets." *Journal of Nuclear Materials* 525(2019):125-139.

Zhou XW and CH Tang. 2011. "Current Status and Future Development of Coated Fuel Particles for High Temperature Gas-cooled Reactors." *Progress in Nuclear Engineering* 53:182-188.

**Pacific Northwest
National Laboratory**

902 Battelle Boulevard
P.O. Box 999
Richland, WA 99354
1-888-375-PNNL (7665)

www.pnnl.gov | www.nrc.gov